POLYTECHNIQUE MONTRÉAL

affiliée à l'Université de Montréal

Evaluation of Mesh Characteristics for Scale-Resolving Simulation of Incompressible Flows

ZAHRA SEIFOLLAHI MOGHADAM

Département de génie mécanique

Mémoire présenté en vue de l'obtention du diplôme de *Maîtrise ès sciences appliquées*
Génie mécanique

Avril 2020

POLYTECHNIQUE MONTRÉAL

affiliée à l'Université de Montréal

Ce mémoire intitulé :

Evaluation of Mesh Characteristics for Scale-Resolving Simulation of Incompressible Flows

présenté par **Zahra SEIFOLLAHI MOGHADAM**
en vue de l'obtention du diplôme de *Maîtrise ès sciences appliquées*
a été dûment accepté par le jury d'examen constitué de :

Jean-Yves TRÉPANIER, président
François GUIBAULT, membre et directeur de recherche
André GARON, membre et codirecteur de recherche
Dominique PELLETIER, membre

ACKNOWLEDGEMENTS

RÉSUMÉ

L'objectif principal de cette recherche est la simulation d'écoulements similaires à ceux rencontrés à l'intérieur des aspirateurs des turbines hydrauliques lorsque celles-ci fonctionnent hors des conditions nominales. L'importance de cette application réside dans le fait que les turbines doivent souvent être exploitées dans une gamme étendue de conditions de fonctionnement, y compris des conditions hors du point du rendement maximum. Ceci s'explique par le fait que l'hydroélectricité joue un rôle important en tant que source flexible d'alimentation en énergie pour le réseau électrique. L'énergie hydro-électrique est particulièrement importante dans la mesure où des sources d'énergie intermittentes telles que l'énergie solaire et éolienne font désormais partie du marché. Cependant, élargir les gammes de conditions de fonctionnement rend plus cruciale l'analyse des contraintes fluctuantes. Celles-ci peuvent en effet entraîner des instabilités, des défaillances mécaniques du système et également des oscillations de puissance spontanées sur le réseau.

Par conséquent, la compréhension et l'atténuation du comportement instable des turbines hydrauliques est centrale. Les approches SRS (Scale Resolving Simulation) telles que les LES et DES ont suscité beaucoup d'intérêt au cours de la dernière décennie pour une compréhension plus complète du comportement opérationnel instable des turbines hydrauliques. Cet intérêt s'explique par leur capacité à résoudre une partie de l'écoulement turbulent. Cependant, pour certains écoulements industriels, comme ceux à charge partielle, à charge partielle profonde ou à vide, pour lesquels les données expérimentales sont insuffisantes pour une compréhension approfondie des phénomènes, la fiabilité des simulations numériques en termes de dépendance au maillage est toujours un problème en suspens. Les études de vérification en LES sont également très difficiles, car les erreurs de discrétisation numérique et de modélisation des échelles sont toutes deux influencées par la résolution du maillage. Un examen approfondi de la littérature montre que les résultats SRS des différentes conditions de fonctionnement des turbines hydrauliques sont encore assez limités et qu'il n'y a pas de consensus sur l'exigence de résolution pour ces études. Par conséquent, le but de cette recherche est de développer un cadre fiable pour la validation et la vérification des études SRS, et plus particulièrement les études LES, afin qu'elles puissent être utilisées pour l'analyse des phénomènes d'écoulement dans les aspirateurs et les roues des turbines hydrauliques, pour des conditions de fonctionnement hors conception.

Plusieurs critères de résolution pour l'analyse LES ont été identifiés dans la littérature et leur applicabilité et leur sensibilité sont examinées. Deux principaux cas test sont considérés dans cette recherche: l'écoulement turbulent dans un canal et un cas d'expansion soudaine.

Dans cette étude, nous n'irons pas plus loin dans les applications aux turbines hydrauliques, mais celles-ci bénéficieront à terme des résultats des recherches en cours.

Les résultats montrent que l'autocorrélation entre deux points est plus sensible à la résolution du maillage que le spectre énergétique. De plus, dans le cas d'une expansion soudaine, la résolution du maillage a un effet énorme sur les résultats et jusqu'à présent, nous n'avons pas capté de comportement de convergence asymptotique dans les résultats de RMS des fluctuations de vitesse et d'autocorrélation en deux points. Ce cas, qui représente un comportement d'écoulement complexe, nécessite d'autres études de résolution de maillage.

ABSTRACT

The central aim of this research is on the simulation of flows similar to the ones which occur inside hydraulic turbine draft-tubes at off-design operating conditions. The importance of this application is due to the fact that hydroturbines often need to be operated over an extended range of operating conditions including off-design conditions, since hydropower plays a significant role as a flexible source of energy supply to the electric network. This significance is due to the integration of non-dispatchable sources of energy such as solar and wind power. This range of operating conditions, however, makes the investigation of fluctuating stresses more crucial. Load fluctuations lead to instability, system mechanical failure and also to spontaneous power swings to the grid. Consequently, understanding and mitigating unsteady operational behavior of hydro turbines is very crucial.

Scale Resolving Simulation (SRS) approaches such as large-eddy simulation (LES) and Detached Eddy Simulation (DES) have received more interests in the recent decade for understanding and mitigating unsteady operational behavior of hydro turbines. This interest is due to the ability of these methods to resolve part of turbulent flow. However, for some industrial flows, where there is no adequate experimental data for deep understanding of the flow physics, such as the ones which happen at part load, deep part load and speed no-load operation of hydraulic turbines, the reliability of numerical simulations in terms of their grid-dependency is still an open question.

Verification studies in LES are also very challenging, since errors in numerical discretization and also subgrid-scale-model are both influenced by grid resolution. Comprehensive examination of the literature shows that the SRS of different operating condition of the hydraulic turbines is still quite limited and that there is no consensus on the resolution requirement of SRS studies. Therefore, the goal of this research is to develop a reliable framework for validation and verification of SRS, specially LES, so that it can be applied for the investigation of flow phenomena in hydraulic turbines draft-tubes and runners at their off-design operating conditions.

Several resolution criteria for LES analysis have been identified in the literature and their applicability and the level of insight which they put into our analysis are scrutinized. Two main test cases are considered in this research, turbulent channel flow and a case of sudden expansion. In this study we will not further go to the real applications and simulations in hydraulic turbines. Hydraulic turbines will eventually benefit from the results of the current research. The results show that two-point autocorrelation is more sensitive to mesh resolution that energy spectra. In addition, for the case of sudden expansion, the mesh resolution has

a tremendous effect on the results and so far, we did not capture an asymptotic converging behaviour in the results of RMS of velocity fluctuations and two-point autocorrelation. This case, which represents complex flow behaviour, needs further mesh resolution studies.

TABLE OF CONTENTS

LIST OF TABLES

LIST OF FIGURES

LIST OF SYMBOLS AND ACRONYMS

ASM	Algebraic Reynolds-stress model
BEP	Best Efficiency Point
CFD	Computational Fluid dynamic
DES	Detached Eddy Simulation
DDES	Delayed Detached Eddy Simulation
DFSEM	Divergence-free synthetic eddy method
DNS	Direct Numerical Simulation
EARSM	Explicit algebraic Reynolds-stress model
EASM	Explicit algebraic stress model
IDDES	Improved Delayed Detached Eddy Simulation
IEA	International Energy Agency
LES	large-eddy simulation
PSD	Power spectral density
RANS	Reynolds-averaged Navier-Stokes
RMS	Root mean square
RSM	Reynolds-stress model
RSTM	Reynolds-stress transport model
SAS	Scale Adaptive Simulation
SGS	sub-grid-scale
SST	Shear Stress Transport
SRS	Scale Resolving Simulation
URANS	Unsteady Reynolds-averaged Navier-Stokes
WALE	Wall-Adapting Local Eddy-viscosity

LIST OF APPENDICES

CHAPTER 1   INTRODUCTION

Hydraulic-turbines are considered a highly reliable power source that can cover an extensive range of operating conditions in response to electricity demand. At different operating conditions of hydraulic-turbines, the flow phenomena include low-frequency and high-frequency pressure fluctuations, depending on turbine flow discharge. Understanding and mitigating these unsteady loads at off-design operating conditions is very crucial to insure the stability and integrity of the turbines. Apart from experimental studies, there is a huge focus on numerical simulations of different configurations of hydro-turbines.

RANS methods are not able to fully capture the turbulent behavior of the flow at off-design operating conditions inside hydro-turbines, as addressed through a comprehensive literature review in this research. Large-eddy simulation (LES) has received more interest in recent years for understanding and mitigating unsteady operational behavior of hydro-turbines. This interest is due to the ability of LES to fully resolve a larger part of flow turbulence as compared to RANS. However, verification studies in LES are very challenging since errors in numerical discretization and also subgrid-scale-model are both influenced by grid resolution. Therefore, the goal of this research is to develop a reliable framework for LES calculations that can be applied for the investigation of flow phenomena in draft-tube and runner of hydraulic turbines at their off-design operating conditions.

1.1   Hydroelectric power

Hydroelectric power has been identified as a reliable source of renewable energy in the last century. As it accounts for approximately one-fifth of the total installed electric capacity worldwide, it has a significant role in the world's energy supply [6]. Figure 1.1 shows the increase in electricity extraction from hydropower from 1971 to 2016. According to the International Energy Agency (IEA), as of 2016, hydro-power contributed to approximately 4170 TWh of the annual world electricity production [3]. Moreover, there is still a great potential for harnessing of existing hydro-power sites.

Integration of renewable energy resources to the grid, must not compromise grid stability. However, power from solar and wind energy resources may cause significant perturbations to the grid, due to the intermittent nature of these resources. Therefore, hydro-turbines are considered as a reliable source to cover an extensive range of operating conditions in response to the electricity demand. In this context, hydraulic turbines are increasingly expected

Figure 1.1 World hydro electricity production from 1971 to 2016 by region (TWh) [3]

to be operated over a wide range of off-design operating conditions. This extensive range of operating conditions induces different dynamic behaviors in various components of the turbine that need to be fully understood and controlled.

Hydraulic turbines are generally categorized as impulse turbines or reaction turbines based on the manner in which the water transfers its energy to the runner. Impulse turbines include Pelton, Turgo and Banki (or crossflow) turbines. The most commonly used reactions turbines are Francis turbines, Kaplan turbines, propeller turbines and Bulb turbines. Deriaz turbines, turbines with a rim generator and reversible pump-turbines are also reaction turbines.

Francis turbines are designed to be operated over a wide range of head, specifically between 80 to 500 m [7]. Francis turbines are the most commonly installed hydraulic units in power plants. Figure 1.2 shows the main parts of a Francis turbine which are a spiral case, stay vanes, guide vanes (wicket gates), runner and draft tube.

In a conventional powerplant, as water is released from an upstream reservoir, it passes through a penstock to the spiral case. Spiral casing helps in changing the axial flow direction to radial and it balances the flow distribution in stay vane channels. The flow direction and rate are then controlled by the stay vanes and guide vanes before reaching the runner. The shape of the runner induces the pressure difference required for its rotational motion. The axis of the runner is connected to the generator shaft for conversion of mechanical power to electrical power. After leaving the runner, part of the remaining kinetic energy of the flow is recovered into static pressure as it passes through the draft tube. Finally water is released to the downstream reservoir.

At the design point of hydraulic turbines, the water enters the draft tube with optimum

Figure 1.2 Francis turbine and its components (source: lecture notes course ENE8280)

swirl. However, at off-design conditions, swirling flow deficit or surplus exists which may induce pressure pulsations. Flow rate is the main factor to characterize the flow phenomena. For a Francis turbine, the relative exit angle of the runner blades is designed for a flow rate that corresponds to the best efficiency point which leads to optimal swirl. At lower flows, the absolute flow angle differs and there is an extra residual swirl in the direction of the runner rotation. At higher flow rates there is a swirl deficit against the direction of the runner rotation. This is illustrated in Figure 1.3. In this figure c_m and c_t are the axial and tangential components of flow velocity c. The velocity components u and w are the peripheral velocity of runner and relative velocity respectively.

In swirling flow, there is usually an inner region with a stagnation zone or dead water core. The vorticity of this region boundary, concentrates in a corkscrew-like vortex filament (vortex rope or torch). The swirl mechanism and, consequently, occurrence of pulsation, is mainly controlled by the turbine flow rate. In addition to the swirl, the pulsation is also affected by the level of cavitation [4]. The following paragraphs describe the different phenomena related to the turbine discharge.

- **Deep part load**
  Deep part load consists of discharge values ranging between 0.25 and 0.4 of the Best Efficiency Point (BEP). Inter-blade cavitation vortices appear at this condition, which intensify the amplitude of pressure pulsations [8].

- **Very low load**

Figure 1.3 Runner exit velocity triangles (a) partial load (b) zero swirl (c) high load [4]

Very low load condition is characterized by discharge values ranging between 0.4 and 0.5 of the values at BEP. The pulsations at this condition only consists of random pulsations with the characteristics of a wide-band noise. The swirl ratio at this condition is high and the vortex rope is replaced by a large number of smaller vortices.

- **Part load**

  In Francis turbines the occurrence of a vortex rope typically happens for a relative discharge range value of 0.5 to 0.85 of the value at the BEP. The pulsation at this operating condition is approximately periodic. Pressure pulsations with low frequency and high amplitude are the source of the dynamic loads at this operating condition.

- **Best Efficiency Point (BEP)**

  Best Efficiency Point is the design condition for the hydraulic turbine. At this condition, the flow is stable and attached, with minimum unsteadiness.

- **Full load (or *high load*)**

  The discharge values of 1.1 of the value at the BEP and above are referred to full load or high load condition. High-amplitude pressure pulsations happen in full load which are mainly due to the rotor-stator interaction [9]. In some turbines, a helical vortex shape prevails at full load which can probably be due to the low axial flow velocity in the hub region [4].

- **Speed no-load**

  Speed no-load is a stand-by mode of the turbine, in which the turbine is rotating at its synchronous speed and is waiting to be connected to the grid. At speed no-load, there is no hydro power extraction by the blades and the available energy dissipates to the environment through friction and vortices. This causes high-amplitude stochastic pressure fluctuations [10].

- **Runaway**

  Runaway is the condition where a turbine can operate at the maximum speed without

load. There is the maximum opening of guide vanes which is due to the failure of the control system. At this condition, the pressure loading on the runner blades is up to three times the pressure loading at BEP [11].

1.2 Elements of the problem

As it will be demonstrated through a comprehensive literature review in the next chapter, LES studies for components of the hydraulic turbines are quite limited. The importance of the LES for off-design operating conditions is due to the fact that RANS studies are mainly capable of accurate flow simulations near the Best Efficiency Point, since optimal swirling flow occurs and the level of turbulence is low. However, at off-design operating conditions, swirling vortices are the main phenomena inside hydraulic turbine draft-tubes and the flow is highly turbulent. Therefore it is necessary to use high fidelity methods such as large-eddy simulation to capture the turbulent fluctuations in the flow. Although the flow phenomena at deep part load and speed-no-load are more complex, in this study we perform simulations for swirling flows similar to the part-load conditions for taking an initial step in LES calculations inside hydraulic turbine components.

In order to circumvent the complexities related to the geometry and other requirements for the boundary conditions of the flow simulation inside hydraulic turbine draft-tube, two academic test cases including internal non-swirling and swirling flows with available DNS and experimental data are chosen. First a case of channel flow which has a simple geometry and includes complex near wall turbulent behavior. Second a sudden-expansion test case which resembles the swirling flow at part load operating condition of a hydraulic turbine draft-tube.

Moreover, the OpenFOAM CFD code implements several Sub-Grid Scale (SGS) models and inlet turbulence generation methods which are being further developed and added to the recent versions. These models need to be evaluated for the simulation of LES problems. Therefore an expertise needs to be developed on how to use the OpenFOAM flow solver to set up, run and validate LES calculations, and this expertise could eventually be applied to simulations for hydraulic turbines components. However, the simulations for hydraulic turbines are not performed as part of the present project. Other aspects of an LES calculation including assessment of mesh resolutions and validating the results versus available DNS or experimental data also need to be thoroughly considered and investigated.

1.3   Research objectives

The central goal of this research is to develop a reliable framework for LES studies for internal flows which resemble the flow inside hydraulic turbine components. This framework mainly considers the mesh resolution and the methods and criteria to evaluate the mesh quality effects on the LES results. Therefore the main objective of this research is:

- To evaluate the mesh resolution for the large-eddy simulations of internal non-swirling and swirling flows

This framework will be also narrowed down to the concept and models implemented in the OpenFOAM open source code. The effect of mesh, boundary conditions, SGS model and methods to assess the simulations will be discussed and further elaborated. Therefore our main objective includes the following sub-objectives:

- To investigate the boundary conditions for the inflow turbulent generations of non-swirling and swirling flows

- To investigate the capabilities of the SGS models in large-eddy simulations of non-swirling and swirling flows

- To identify the mesh resolutions criteria and evaluate their capabilities in giving the required insight into the LES problems of interest

1.4   Master's thesis plan

In the present document, Chapter 2 covers a literature review on the history of simulation and modeling of turbulent flow and then the history of turbulent flow simulations inside components of hydraulic turbines. Chapter 3 covers the mathematical description of LES, filtering, description of several SGS models, inlet turbulence generation methods in LES and an identification of methods and criteria for assessment of LES mesh resolution in the literature. In Chapter 4 the selected tests cases are described and the results of the LES for those cases are verified and validated. Chapter 5 is dedicated to the summary and conclusion of this research.

CHAPTER 2   LITERATURE REVIEW

As it was summarized, the flow phenomena in hydraulic turbines include highly swirling flow and low-frequency and high-frequency pressure fluctuations at different operating modes, depending on turbine flow discharge. Understanding and mitigating these unsteady loads at off-design operating conditions in hydraulic turbines is very crucial for stable delivery of hydropower to the grid. Apart from experimental studies, there is a huge focus on numerical simulations of different configurations of turbines, including component modeling and complete turbine modeling at different operating condition of turbines. There is a range of numerical approaches for turbulent flow simulation and modeling. The following section covers a brief history of approaches to turbulent flow simulation from RANS to LES. The next section covers a literature review of the application of these approaches to the numerical flow simulations in components of hydraulic turbines.

2.1   A review of the numerical approaches in studies of turbulent flows

The instantaneous Navier-stokes equations, which represent the motion of an incompressible fluid, are:

$$\frac{\partial U_i}{\partial x_i} = 0 \tag{2.1}$$

$$\frac{\partial U_j}{\partial t} + U_i \frac{\partial U_j}{\partial x_i} = \nu \frac{\partial^2 U_j}{\partial x_i \partial x_i} - \frac{1}{\rho} \frac{\partial p}{\partial x_j} \tag{2.2}$$

Where, ν is the kinematic viscosity ($\nu = \mu/\rho$)

In Direct Numerical Simulation (DNS), the instantaneous Navier-Stokes equations are solved and all scales (i.e. from the integral length and time scales to the Kolmogorov microscales) of the turbulence are calculated. Therefore, this method is very computationally expensive and limited to simple flows.

In large-eddy simulation (LES), large-eddies of the flow are solved (or simulated). In this method, the 'filtered' Navier-stokes equations are solved. These equations contain an additional term that accounts for the effects of the small-scale eddies, which are smaller than the filter size, on the large-scale eddies. A sub-grid-scale (SGS) model is required for this additional term.

Finally in RANS methods, none of the turbulent motions of the flow are directly calculated and only their effect on the mean flow is quantified through the Reynolds-stresses. A model, is therefore required to relate Reynolds-stresses to mean flow quantities.

2.1.1 RANS approaches

When the mean momentum equations (or the averaged, Reynolds-decomposed Navier-stokes equations) are written, additional term $\langle u_i u_j \rangle$ appear:

$$\frac{\partial \langle U_j \rangle}{\partial t} + \langle U_i \rangle \frac{\partial \langle U_j \rangle}{\partial x_i} = \nu \frac{\partial^2 \langle U_j \rangle}{\partial x_i \partial x_i} - \frac{1}{\rho} \frac{\partial \langle p \rangle}{\partial x_j} - \frac{\partial \langle u_i u_j \rangle}{\partial x_i} \tag{2.3}$$

Here the Reynolds decomposition is such that the instantaneous velocity U_i is decomposed into the mean value $\langle U_i \rangle$ and fluctuating value u_i:

$$U_i = \langle U_i \rangle + u_i \tag{2.4}$$

This is the source of the closure problem of the Reynolds-averaged Navier-stokes equations. To solve the equations, an expression for the Reynolds stresses in terms of known quantities is necessary. Such expressions are called closure models which are mainly i) turbulent viscosity (or eddy viscosity) models and ii) Reynolds-stress models.

Turbulent-viscosity models

In turbulent viscosity models, Reynolds stresses are modeled using turbulent viscosity (ν_t):

$$\langle u_i u_j \rangle = \frac{2}{3} k \delta_{ij} - \nu_t \left(\frac{\partial \langle U_i \rangle}{\partial x_j} + \frac{\partial \langle U_j \rangle}{\partial x_i} \right) \tag{2.5}$$

Expressions for ν_t generally take the form $\nu_t = u^\star l^\star$, where $u^\star$ and $l^\star$ are appropriate velocity and length scales. These models include "zero-equation" models (which includes the uniform-turbulent-viscosity model and the mixing-length model), one-equation models and two-equation models.

Zero and one-equation models suffer from their dependency on the flow for the determination of velocity and length scales. This problem is overcome in two-equation models. Two-equation models are the most popular type of the turbulence models. These models incorporates two differential model equations in the specification of $u^\star$ and $l^\star$ which can be given by the expression based on k and ϵ which are the turbulent kinetic energy and the rate

of dissipation of turbulent kinetic energy. $k - \epsilon$ model developed by Launder and Spalding (1979) [12], is the most widely used turbulence model.

Other two-equation models also exist, e.g the $k - \omega$ model developed by Wilcox (1993) [13] (where $\omega \equiv \frac{\epsilon}{k}$ and has the same units as vorticity: time^{-1}) which is superior to the $k - \epsilon$ model in its treatment of near-wall regions and its ability to account for streamwise pressure gradients. However, its treatment of non-turbulent free-stream boundary conditions is problematic, because this model is dependent on the free stream value for ω.

Shear Stress Transport (SST) by Menter (1994) [14] is a combination of $k - \epsilon$ and $k - \omega$ models which applies the $k - \omega$ model in the inner boundary layer and $k - \epsilon$ model in the outer region of the boundary layer as well as outside of it. Therefore with this model, both $k - \epsilon$ and $k - \omega$ models are improved.

Spalart and Allmaras (1994) [15] also described a one-equation model developed for aerodynamic applications, in which a single model transport equation is solved for the turbulent viscosity ν_t.

Reynolds-stress models

In Reynolds-stress models, the difficulties associated with turbulent viscosity models are avoided by solving a modelled transport equation for each component of the Reynolds stresses. These models are called Reynolds-stress model (RSM) or Reynolds-stress transport model (RSTM). In Algebraic Reynolds-stress model (ASM), algebraic equations are solved for the Reynolds-stresses. There are also explicit algebraic Reynolds-stress models (Explicit ASM or EASM or EARSM) in which explicit algebraic equations are solved for the Reynolds-stresses [16]. These models although take into account the anisotropy of the turbulence by solving all the components of the turbulent transport, they are more computationally expensive in comparison with one- or two- equation models.

2.1.2 DES: detached-eddy simulation

DES aims at capturing the boundary layer with Unsteady RANS (Unsteady Reynolds-averaged Navier-Stokes (URANS)) and the outer detached eddies with LES. The reason to use DES is to avoid very fine grid resolutions near the wall. The RANS model that was originally used in the DES was the one-equation Spalart and Allmaras (SA) model [17]. DES based on two-equation models were also proposed for $k - \omega$ SST [18]. For high Reynolds number flows, LES requires very fine grids near the walls. To circumvent this problem for large industrial cases and to reduce simulation time, DES is widely used.

In some cases the DES model switches to LES in the boundary layer, therefore the boundary layer is treated in LES mode with a coarse mesh not suitable for LES, resulting in a poor LES. Delayed DES (Delayed Detached Eddy Simulation (DDES)) is proposed to protect the boundary layer from LES mode.

Hybrid RANS-LES [19] is also similar to DES. The only difference is that the Hybrid RANS-LES only covers the inner part of the boundary layer with URANS. More mathematical modelling on LES itself will be explained in section 3.5.

2.1.3 SAS: Scale Adaptive Simulations

Scale Adaptive Simulation (SAS) is a way to improve a RANS model ability to resolve large-scale motions in the flow in unsteady mode. However, this model resolves less turbulence than LES. This model does not use the filter-width as a length scale. Menter and others (2003) [20], developed a one-equation turbulent-viscosity model in which they used the von-Karman length scale. This length scale, which includes the second derivative of velocity, is a suitable length scale for detecting unsteadiness. This model was called the SAS model. In [21] they improved the k-ω-SST model to include the SAS features. This model was called SST-SAS.

2.1.4 Large-eddy simulation

The history of large-eddy simulation goes back to its initial proposition by Smagorinsky (1963) for the simulation of atmospheric air currents [22]. It was then explored by Deardorff (1970) for channel flow simulation [23]. LES is being widely used for simulation of problems in combustion, acoustic and atmospheric boundary layer. In large-eddy simulations, the large eddies are fully resolved in time and space and the effect of the smaller eddies, quasi-universal eddies, on the larger ones are modeled. These models which are called sub-grid-scale models, are generally a turbulent viscosity method. Since LES fully resolves the large-scale eddies, it is more accurate than a RANS approach, especially in flows where large-scale unsteadiness is present (e.g. vortex shedding, boundary layer separation, etc.). A thorough mathematical description of LES and a description of the well-knows SGS models such as Smagorinsky, WALE, one equation k model and dynamic model is presented in the next chapter.

2.2 Literature review on numerical simulations for hydraulic turbines

Analysis of flow phenomena for different components of hydraulic turbines has been performed by a large number of researchers in the last few decades. Flow physics in different components

of hydraulic turbines vary over their range of operating conditions which go from the speed-no load condition to full load. The choice of turbulence models in numerical studies is restricted by the computational resources and the expected level of accuracy of the results. The following sections cover a literature review on the URANS, DES, SAS and LES studies for hydraulic turbines.

2.2.1 URANS studies

The URANS is the most common approach used by researchers for numerical analysis of the flow field in hydraulic turbines. Ciocan et al. (2007) studied the dynamics of the vortex rope for the FLINDT draft tube at part load experimentally and numerically [24]. The URANS numerical approach with the k-ϵ turbulence model was used to validate results of vortex precession frequency, phase average wall pressure, mean velocity profiles in the cone and the center of vortex against experimental data. In this study, 3% error for pressure pulsation amplitude and 13% error for vortex frequency is reported for estimating the accuracy of the prediction for the vortex global quantities (i.e. vortex frequency and amplitude of pressure fluctuations).

A similar study for the same test case was performed by Vu et al. (2010) and draft tube recovery factor from part load to full load is compared with experimental data. The suitability of circumferentially averaged inlet conditions for draft tube is proven to be satisfactory in this research for the estimation of the global performance characteristics of the machine [25]. The limitation of URANS in predicting self-induced vortex rope is reported by Foroutan and Yavuzkurt (2012) and the importance of time-dependent boundary conditions with turbulent fluctuations at the inlet of the draft tube has been shown [26].

URANS is also used by Nicolle et al. (2012) for speed no-load condition and the pressure fluctuations at the runner leading edge is compared with experimental data. The limitation of this numerical simulation to capture the initial double peak associated with the motion of the stagnation point is presented in this study [27].

URANS simulation of a pump-turbine at speed no-load and runaway condition, is also performed by Casartelli et al. (2014), Gentner et al. (2014) to investigate S-shape characteristics [28, 29]. Nicolle et al. (2014) investigated the rotating stall phenomenon for a Francis turbine [30]. Hosseinimanesh et al. (2016) also compared the results of URANS simulation of a Francis turbine at no-load condition with experimental data for pressure fluctuations and they showed that URANS is not able to capture all details of the flow physics at this flow condition [31].

2.2.2 SAS studies

SAS, due to its capability to dynamically adjust the length scale in the turbulent flow and hence provide more detailed predictions of turbulent flow structures, is often employed for draft tube flow field behavior investigations. For instance in a study by Neto et al. (2012), SAS-SST results of velocity components inside a draft tube are validated against experimental data for a Francis turbine at part load [32].

The same approach is applied by Vu et al. (2012) for the AxialT turbine at BEP and part load together with the validation of pressure fluctuations [33]. Krappel et al. (2014) compared the results of SAS-SST with RANS-SST and investigated the effect of mesh [34] and the pressure fluctuation data are also validated [35]. The results of SST-SAS analysis is used by Pasche et al. (2017) for stability analysis of the FLINDT draft tube vortex rope at part load condition [36].

2.2.3 DES (Hybrid) studies

DES as a Hybrid RANS/LES approach, applies the RANS approach for near wall modeling of turbulence and resolves the core flow region using LES. This method is applied by Magnoli and Schilling (2012) for a range of flows, including deep part load, higher part load, part load and full load of Francis turbines. Pressure field history is used for assessment of dynamic stresses at the runner [37].

The same approach is employed by Sentyabov et al. (2014) for the analysis of vortex core precession of a Kaplan turbine. They compared their results for different variations of DES (k-ω SST, Spalart Almaras DES, k-ω SST DDES) with the results of k-ω SST URANS. They concluded that the precession frequency is identical for all the methods and that only the details of the flow differ. Due to the dissipative behavior of URANS, there is an underestimation of pressure fluctuations [38]. The results of the turbulent kinetic energy of DES inside draft tube is also compared with URANS by Foroutan and Yavuzkurt (2012) and its capability in better predicting the turbulent kinetic energy is shown [26].

A comparison of URANS and DES potentials to predict turbulence statistics for the draft tube is presented by Paik et al. (2005). Although both methods agree in mean velocity field, the results of turbulence statistics show significant discrepancies for URANS [39]. DES is used for the prediction of pressure pulsation in high-head Francis turbines by Minakov et al. (2015) and an accuracy of 10% is reported for the simulations [40].

The DDES method for testing the effect of different methods for generating inflow turbulence as several variations of Artificial Fluctuation Generation (AFG) was studied for the

BulbT turbine by Taheri (2015). In this study it is shown that although the effect of inflow turbulence modifies the prediction of separation dynamics, it has little effect on global quantities [41].

2.2.4 LES studies

In recent decades, by the development of super computers, LES has been used by several researchers for the investigation of swirling flows. The instantaneous results of velocity in a conical diffuser using LES with wall modeling as a function of local velocity and local pressure gradients and using the recycling method for inflow turbulence is presented in a study by Duprat et al. (2009) [42].

Several turbulence study approaches including SAS-SST, RSM and LES for validation of the results of cavitating and non-cavitating vortex rope at part load are also presented in a study by Jost and Lipej (2011) [43]. In this paper, vortex rope frequency and pressure amplitude is compared against experimental data. It has been shown that when cavitation is modeled, the results of the LES show better agreement with the experimental data. Another study of the combined LES and cavitation model is also performed by Su et al. (2013) and pressure fluctuations for both cavitation model and single phase model are compared with experimental data [44]. The results of this study show that the high frequency component at the inlet of draft tube can be predicted by using a cavitation model.

A comparison of LES and SAS results for a sudden-expansion test case which resembles the vortex rope of a draft tube at part load is performed by Javadi and Nilsson (2014) [45]. Rotating stall mechanism of a pump-turbine is investigated by Pacot et al. (2014) using LES [46]. The results of efficiency prediction of a Kaplan turbine using Zonal LES (ZLES) is compared to SAS in a study by Morgut et al. (2015) [47].

LES with a cavitation model at part load is also implemented by Pacot et al. (2015) for the investigation of pressure pulsations and it is reported that the predicted value for the amplitude of fluctuations did not agree well with the experiment with 35% error [48]. Dynamic loads of a model Francis turbine at speed no-load conditions for fatigue analysis is investigated using SAS-SST and LES by Mende et al. (2016) [49]. Comparison of head losses for a bulb turbine draft tube at BEP and high load conditions using LES and URANS is also performed by Wilhelm et al. (2016) to better understand the origin of losses [50, 51].

LES with a cavitation model for Francis turbine is also performed at part load and high load in a study by Yang et al. (2016). In this study, however, the LES mesh requirements were not well-satisfied [52]. Comparison of LES results with DES and URANS results for Francis-

99 draft tube at part load, BEP and high load is performed by Minakov et al. (2017) for mean velocity profiles and pressure fluctuations [53, 54]. Compressible LES is performed by Trivedi and Dahlhaug (2018) for a whole configuration of the Francis-99 turbine to compare the high-amplitude stochastic fluctuations at speed no-load [10] and runaway [55]. In the paper at runaway condition, they use grid convergence index, index of resolution quality and Pope's criterion (M) for mesh resolution and uncertainty quantification.

A review of LES and DES studies of hydraulic turbines is presented in Table 2.1 to the Table 2.4 respectively. In the papers featuring LES study for hydraulic turbine, the effect of the mesh was barely studied. Moreover, as it is also clear from the tables, there is no consensus on the resolution requirements for the LES or DES studies in terms of the mesh resolution and time step. The validation studies in most of the references are less than adequate, since most of the studies avoid to validate the turbulent characteristics of the flow. This points to a choice of academic test cases with proper DNS or experimental validation data.

Table 2.1 Part 1: review of references on LES of hydraulic turbines (SGS = Sub-grid Scale Model, WALE = Wall-Adapting Local Eddy)

Ref	Year	Author	Turbine type	Component	Operating condition	Phenomena	Solver	SGS model
[55]	2018	Trivedi and Dahlhaug	Francis	Whole	runaway	vortex rings in blade cascades	CFX	WALE
[10]	2018	Trivedi	Francis	Whole	SNL	rotor -stator interaction	CFX	WALE
[54]	2017	Minakov et al.	Kaplan	GV /R /DT	low load	vortex ropes	Fluent	WALE
[53]	2017	Minakov et al.	Francis	Whole	PL/ BEP /HL	vortex ropes	Fluent	WALE
[52]	2016	Yang et al.	Francis	Whole	PL/HL	vortex ropes /w cavitation		
[51]	2016	Wilhelm et al.	Bulb	DT	PL/ BEP/ HL	Head losses	YALES2	dynamic Smagorinsky
[49]	2016	Mende et al.	Francis	Whole	SNL	Dynamic loads	AcuSolve	dynamic Germano
[48]	2015	Pacot et al.	Francis	Whole	PL	vortex rope	FrontFlow/blue	dynamic Smagorinsky
[46]	2014	Pacot et al.	pump-turbine	Whole	PL	Rotating-stall	FrontFlow/Blue	dynamic Smagorinsky
[44]	2013	Su et al.	Francis	Whole		vortex rope w/ cavitation		Smagorinsky
[43]	2011	Jost and Lipej	Francis	DT	PL	vortex rope w/ cavitation	CFX	WALE

Table 2.2 Part 2: review of references on LES of hydraulic turbines (SGS = Sub-grid Scale Model, WALE = Wall-Adapting Local Eddy)

Ref	Year	Author	Temporal scheme	Advection scheme	Time step	Number of nodes	Inlet BC	Outlet BC	Validation
[55]	2018	Trivedi and Dahlhaug	Euler	bounded central -difference	10^{-5} s	72×10^6			Power spectra
[10]	2018	Trivedi	second-order backward Euler	bounded central -difference	10^{-7} s	36.88×10^6	Total pressure	Static pressure	Pressure pulsation
[54]	2017	Minakov et al.	implicit second-order	second-order central	CFL < 2	19.3×10^6	Random fluctuations	Convective outflow	Pressure fluctuation /Mean velocity/ k
[53]	2017	Minakov et al.	implicit second-order	second-order central	CFL < 2	14.28×10^6	Random fluctuations/ Total head		Mean velocity/ Pressure fluctuations
[52]	2016	Yang et al.		second-order central	1° runner revolution	1.6×10^6	Total pressure	Static pressure	Pressure pulsation
[51]	2016	Wilhelm et al.	4th order	4th order	0.07° runner revolution	4.7×10^6	Mass flow/ Inlet unsteady profile	Static pressure	Mean velocity /Reynolds stresses
[49]	2016	Mende et al.	second order	second order	0.048° runner revolution	105×10^6	Time averaged velocity field	Pressure	Pressure fluctuations
[48]	2015	Pacot et al.	implicit Crank-Nicolson	Galerkin Finite Element	3.1×10^{-6} s	123×10^6	Uniform velocity	Traction free	
[46]	2014	Pacot et al.	implicit Crank-Nicolson	Galerkin Finite Element		85×10^6			Energy coefficient
[44]	2013	Su et al.			0.0002 s	8×10^6	Total pressure	static pressure	Pressure fluctuation
[43]	2011	Jost and Lipej			0.5° runner revolution	23.5×10^6	Velocity profile	static pressure	Pressure pulsation

Table 2.3 Part 1: review of references on DES/DDES/IDDES of hydraulic turbines (SGS = Sub-grid Scale Model)

Ref	Year	Author	Turbine type	Component	Operating condition	Phenomena	Solver	Model	SGS model
[53]	2017	Minakov et al.	Francis	Whole	PL/ BEP /HL	vortex rope	Fluent	DES $k - \omega$ SST	
[56]	2017	Javadi and Nilsson	Kaplan	Whole	PL/ BEP	Rotor-stator interaction/ vortex rope	OpenFOAM	DDES S-A	
[57]	2017	Gavrilov et al.	Francis	DT	PL	vortex rope	σFlow	Hybrid RANS-LES	SGS-k
[58]	2015	Krappel et al.	Francis	Whole	PL	vortex rope	OpenFOAM	IDDES-SST	
[41]	2015	Taheri	Bulb	DT	PL/ BEP /HL	vortex rope separation/ runner related vortical structures	CFX OpenFOAM	DDES S-A	Smagorinsky
[40]	2015	Minakov et al.	Francis	Whole		vortex rope	Fluent	DES $k - \omega$ SST	
[59]	2014	Foroutan and Yavuzkurt	Francis	DT	PL	vortex rope		DDES $k - \omega$ SST	
[38]	2014	Sentyabov et al.	Kaplan	DT	PL	vortex rope		DES/DDES $k - \omega$ SST	
[60]	2014	Jost et al.	Kaplan	Whole	PL/ BEP /HL		CFX	ZLES	
[61]	2014	Jošt and Škerlavaj	Bulb	Whole	PL/ BEP /HL		CFX	ZLES	
[37]	2012	Magnoli and Schilling	Francis	Whole	PL/HL/ Deep PL Higher PL	rotor-stator interaction/ vortex rope		DES $k - \omega$ SST	
[26]	2012	Foroutan and Yavuzkurt	Francis	DT	PL	vortex rope	Fluent OpenFOAM	DES $k - \epsilon$ Realizable	
[39]	2005	Paik et al.		DT		spiral rope vortex		DES S-A	

Table 2.4 Part 2: review of references on DES/DDES/IDDES of hydraulic turbines (SGS = Sub-grid Scale Model)

Ref	Year	Author	Temporal scheme	Advection scheme	Time step	Number of nodes	Inlet BC	Outlet BC	Validation
[53]	2017	Minakov et al.	implicit second-order	second-order central	CFL < 2		Random fluctuations/ Total head		Mean velocity/ Pressure fluctuations
[56]	2017	Javadi and Nilsson	implicit second-order	blended scheme	CFL=0.001	40×10^6	Constant bulk velocity	Neumann	Mean and RMS velocity
[57]	2017	Gavrilov et al.	Crank–Nicolson	high-order central difference	CFL=0.3	5.6×10^6	Precursor RANS	Non-reflecting	
[58]	2015	Krappel et al.	second order backward Euler	bounded second order central difference	0.25° runner revolution	20×10^6	recycled method		Mean velocity/ Pressure pulsation
[41]	2015	Taheri	Backward	Upwind	0.63° runner revolution	7.26×10^6	Axisymmetric and 2D velocity profile/ Artificial fluctuation	fixed MeanValue (zero) for P and zeroGradient for the rest	Mean velocities/ recovery coefficient/ k/ Energy spectra
[40]	2015	Minakov et al.	implicit second-order	Quick scheme	0.05 s	5×10^6			Discharge/ Pressure pulsation
[59]	2014	Foroutan and Yavuzkurt	implicit second-order	bounded central-difference	CFL=0.0044	3.36×10^6	Mean velocity profile		
[38]	2014	Sentyabov et al.		Quick	0.001 s	1.25×10^6	Inlet velocity profile	constant derivative along the normal for P and zero derivative along the normal for the rest	Precession frequency
[60]	2014	Jost et al.	second-order backward Euler	bounded central difference	0.5° runner revolution	8×10^6			Efficiency
[61]	2014	Jošt and Škerlavaj	second-order backward Euler	bounded central difference	0.5° runner revolution	9×10^6			Efficiency
[37]	2012	Magnoli and Schilling		central/ upwind difference					pressure oscillation amplitude
[26]	2012	Foroutan and Yavuzkurt			1° runner revolution	2×10^6	time -dependent	radial equilibrium condition	Mean velocity k
[39]	2005	Paik et al.	second-order	second-order	local pseudotime stepping	1.8×10^6	steady /axisymmetric	Nonreflecting characteristics -based	mean velocity profiles

CHAPTER 3   SIMULATION AND MODELING OF TURBULENT FLOW

As stated previously, the instantaneous Navier-stokes equations, which represent the motion of an incompressible fluid, are:

$$\frac{\partial U_i}{\partial x_i} = 0 \tag{3.1}$$

$$\frac{\partial U_j}{\partial t} + U_i \frac{\partial U_j}{\partial x_i} = \nu \frac{\partial^2 U_j}{\partial x_i \partial x_i} - \frac{1}{\rho} \frac{\partial p}{\partial x_j} \tag{3.2}$$

Where, ν is the kinematic viscosity ($\nu = \mu/\rho$)

3.1   Mathematical description of LES

In LES, the velocity field (U_i) is decomposed into a filtered (or resolved) component ($\overline{U_i}$) and a residual (or sub-grid scale, SGS) component (u'). This decomposition is done by applying a filtering operator to the Navier-Stokes equations. The general filtering operation is mathematically expressed as a convolution of the relevant flow field with a chosen filter kernel:

$$\overline{\boldsymbol{U}}(\boldsymbol{x},t) = \int G(\boldsymbol{x} - \boldsymbol{r}, \boldsymbol{\Delta}) \boldsymbol{U}(\boldsymbol{x},t) d\boldsymbol{r}, \tag{3.3}$$

where integration is over the entire flow domain, and the specified filter function G satisfies the normalization condition

$$\int G(\boldsymbol{r}, \boldsymbol{x}) d\boldsymbol{r} = 1. \tag{3.4}$$

The filter most commonly used in conjunction with a finite volume discretization is the top-hat filter, in which filtering gives a value which is an average over a rectangular volume Δ^3, where Δ is the filter width.

$$G(\boldsymbol{x} - \boldsymbol{r}, \boldsymbol{\Delta}) = \begin{cases} 1/\Delta^3, \ |\boldsymbol{x} - \boldsymbol{r}| \leq \Delta/2 \\ 0 \ \text{otherwise.} \end{cases} \tag{3.5}$$

A common choice for Δ is the cubic root of the volume of the computational cell,

$$\Delta = \sqrt[3]{\Delta x \Delta y \Delta z} \tag{3.6}$$

where Δx, Δy and Δz are the cell-sizes along the corresponding coordinate axes. This choice of Δ conveniently makes $\overline{U}$ equal to the average value of U in the computational cell. This implies that no explicit filtering needs to be performed during the computational procedure, instead the filtering is built into the discretization method itself.

Therefore:

$$U_i = \overline{U_i} + u_i' \tag{3.7}$$

This is analogous to the Reynolds decomposition. Important differences, however, are that $\overline{U_i}$ is a random field, and that (in general) the filtered residual is not zero $(\overline{u_i'} \neq 0)$. However, by definition, the average of fluctuating velocities are zero $(\langle u_i \rangle = 0)$. A comparison between averaging in RANS and filtering in LES is shown in Figure 3.1.

Figure 3.1 A comparison of filtering and averaging of the instantaneous velocity data [5]

By formally applying the filtering operation to the continuity equation and Navier-Stokes equations, it is possible to derive conservation laws for the filtered flow variables. Due to the linearity of the continuity equation, applying the filtering is straightforward. The form of the equation remains unchanged.

$$\frac{\partial \overline{U_i}}{\partial x_i} = 0 \tag{3.8}$$

The resulting Navier-stokes equations are of the same form as the original Navier-stokes equations and also a residual stress tensor or SGS stress tensor (τ_{ij}^r) appears:

$$\frac{\partial \overline{U_j}}{\partial t} + \overline{U_i}\frac{\partial \overline{U_j}}{\partial x_i} = \nu \frac{\partial^2 \overline{U_j}}{\partial x_i \partial x_i} - \frac{1}{\rho}\frac{\partial \overline{p}}{\partial x_j} - \frac{\partial \tau^r_{ij}}{\partial x_i} \tag{3.9}$$

The appearance of this residual stress tensor is due to the fact that the filtered product $\overline{U_i U_j}$ is different from the product of the filtered velocities $\overline{U}_i\overline{U}_j$. The difference is the *residual-stress tensor* defined by:

$$\tau^R_{ij} \equiv \overline{U_i U_j} - \overline{U}_i\overline{U}_j, \tag{3.10}$$

The *residual kinetic energy* is:

$$k_r \equiv \frac{1}{2}\tau^R_{ii}, \tag{3.11}$$

and the *anisotropic residual-stress tensor* is defined by

$$\tau^r_{ij} \equiv \tau^R_{ij} - \frac{2}{3}k_r\delta_{ij}. \tag{3.12}$$

The isotropic residual stress is included in the modified filtered pressure

$$\overline{p} \equiv \overline{p} + \frac{2}{3}\rho k_r. \tag{3.13}$$

3.2 Residual-stress models in LES

The equation of motions must be closed by modeling the SGS stress tensor. This is usually performed using an eddy viscosity model.

3.2.1 The Smagorinsky model

The simplest model for (τ^r_{ij}) was proposed by Smagorinsky (1963) [22] in which the residual stress is related to the filtered rate of strain $\left(\overline{S}_{ij} \equiv \left(\frac{\partial \overline{U_i}}{\partial x_j} + \frac{\partial \overline{U_j}}{\partial x_i}\right)\right)$.

$$\tau^r_{ij} = -2\nu_r\overline{S}_{ij}, \tag{3.14}$$

where

$$\nu_r = l_S^2(2\overline{S}_{ij}\overline{S}_{ij})^{1/2} \tag{3.15}$$

and

$$l_S = C_S \Delta, \tag{3.16}$$

Where $C_S \approx 0.17$ is the Smagorinsky coefficient and the Smagorinsky length scale, l_S, is taken to be proportional to the filter width, Δ. The main deficiency of the Smagorinsky model is that its eddy-viscosity does not go to zero for laminar shear flows.

3.2.2 The WALE model

The WALE model of Nicoud and Ducros [62], handles this problem by controlling the eddy-viscosity in laminar flow. Therefore, this model is also capable of computing flows with laminar-turbulent transition. In this model, the eddy-viscosity reads as:

$$\nu_r = (C_w \Delta)^2 \frac{(S_{ij}^d S_{ij}^d)^{3/2}}{(\overline{S}_{ij} \overline{S}_{ij})^{5/2} + (S_{ij}^d S_{ij}^d)^{5/4}} \tag{3.17}$$

where

$$S_{ij}^d = \frac{1}{2}(\overline{g}_{ij}^2 + \overline{g}_{ji}^2) - \frac{1}{3}\delta_{ij}\overline{g}_{kk}^2$$
$$\overline{g}_{ij} = \frac{\partial \overline{U}_i}{\partial x_j} \tag{3.18}$$
$$\overline{g}_{ij}^2 = \overline{g}_{ik}\overline{g}_{kj}$$

and the constant is in the range $0.55 \leq C_w \leq 0.60$.

3.2.3 The k-equation model

A one-equation model can be used to model SGS turbulent kinetic energy:

$$\frac{\partial k_{sgs}}{\partial t} + \frac{\partial(\overline{U}_j k_{sgs})}{\partial x_j} = \frac{\partial}{\partial x_j}\left[(\nu + \nu_{sgs})\frac{\partial k_{sgs}}{\partial x_j}\right] + P_{k_{sgs}} - \epsilon \tag{3.19}$$

$$\nu_{sgs} = c_k \Delta k_{sgs}^{1/2} \tag{3.20}$$

$$\epsilon = C_\epsilon \frac{k_{sgs}^{3/2}}{\Delta} \tag{3.21}$$

$$P_{k_{sgs}} = 2\nu_{sgs}\overline{S}_{ij}\overline{S}_{ij} \tag{3.22}$$

Very close to the wall, the van Driest damping function is used to correct the behavior for the ν_{sgs}. This function has the following form:

$$D = 1 - e^{\frac{-y^+}{A^+}} \tag{3.23}$$

where $A^+ = 26$. The final length scale is given by:

$$\Delta = min(\frac{\kappa y}{C_S}D, \Delta_g) \tag{3.24}$$

where Δ_g is a geometric-based filter length such as the cube-root volume delta.

3.2.4 The dynamic model

In the dynamic model of Germano and others (1991) [63], the C_S constant is not chosen, it is computed. The dynamic model provides a methodology for determining an appropriate local value of the Smagorinsky coefficient. The dynamic model involves filters of different filter widths. The *grid filter* has filter width $\overline{\Delta}$ and the operation of grid filtering is denoted by an overbar ($\overline{U}$). The LES equations are deemed to be solved for $\overline{U}_i$, although this filtering operation is not explicitly performed. The test filter has filter width $\tilde{\Delta}$, which is typically taken to be twice $\overline{\Delta}$ and test filtering is denoted by a tilde ($\tilde{U}$).

The residual stresses based on the single- and double-filtering operations are defined by

$$\tau_{ij}^R \equiv \overline{U_iU_j} - \overline{U}_i\overline{U}_j, \tag{3.25}$$

$$T_{ij} \equiv \widetilde{\overline{U_iU_j}} - \widetilde{\overline{U}_i}\widetilde{\overline{U}_j}. \tag{3.26}$$

Using Germano identity we define $\mathcal{L}_{ij}$ which relates the two subgrid-scale stresses by:

$$\mathcal{L}_{ij} \equiv T_{ij} - \widetilde{\tau_{ij}^R} = \widetilde{\overline{U}_i\overline{U}_j} - \widetilde{\overline{U}_i}\widetilde{\overline{U}_j} \tag{3.27}$$

It has to be mentioned that $\mathcal{L}_{ij}$– which is called the *resolved stress* – is known in terms of $\overline{U}$, whereas T_{ij} and τ_{ij}^R are not.

The Smagorinsky model for the deviatoric parts τ_{ij}^r and T_{ij}^d are:

$$\tau_{ij}^r \equiv \tau_{ij}^R - \frac{1}{3}\tau_{kk}^R \delta_{ij} = -2c_S \overline{\Delta}^2 \overline{\mathcal{S}}\ \overline{S}_{ij} \tag{3.28}$$

$$T_{ij}^d \equiv T_{ij} - \frac{1}{3}T_{kk}\delta_{ij} = -2c_S \widetilde{\overline{\Delta}}^2 \widetilde{\overline{\mathcal{S}}}\ \widetilde{\overline{S}}_{ij}, \tag{3.29}$$

where $\overline{S}$ is the characteristic filtered rate of strain defined by:

$$\overline{\mathcal{S}} \equiv \left(2\overline{S}_{ij}\overline{S}_{ij}\right)^{1/2} \tag{3.30}$$

Note that the coefficient has been redefined as c_S for the possibility of negative values. By defining

$$M_{ij} \equiv 2\overline{\Delta}^2 \widetilde{\overline{\mathcal{S}}\ \overline{S}_{ij}} - 2\widetilde{\overline{\Delta}}^2 \widetilde{\overline{\mathcal{S}}}\ \widetilde{\overline{S}}_{ij} \tag{3.31}$$

The Smagorinsky model for the the deviatoric part of $\mathcal{L}_{ij}$ ($\mathcal{L}_{ij}^d \equiv \mathcal{L}_{ij} - \frac{1}{3}\mathcal{L}_{kk}\delta_{ij}$) will be

$$\mathcal{L}_{ij}^S \equiv T_{ij}^d - \widetilde{\tau_{ij}^r} = c_S M_{ij}. \tag{3.32}$$

In a LES, M_{ij} and $\mathcal{L}_{ij}$ are known in terms of $\overline{U}_i$, therefore the value of the Smagorinsky coefficient c_S can be determined. Lilly (1992) [64] modified the constant by:

$$c_S = \frac{M_{ij}\mathcal{L}_{ij}}{M_{kl}M_{kl}}. \tag{3.33}$$

3.3 Inlet boundary conditions for LES

In RANS simulations, it is sufficient to provide the mean inlet profiles and the turbulent quantities. However, while performing an unsteady simulation, the time history of the velocity needs to be specified, which includes the turbulent fluctuations. The turbulent inlet condition for the LES should meet some or all of the following criteria [1]:

- Stochastical variation;

- Including all the scales down to the filter scale (spatially and temporally);

- Compatibility with Navier–Stokes equations;

- 'Look' like turbulence;

- Easy specification of turbulent properties as turbulence intensities, length scales, etc;

- Easy implementation and adjustment.

The ways to create turbulent inlet boundary conditions vary and include the two main categories of synthesis inlets and precursor simulation methods which are briefly described in the following sections.

3.3.1   Synthesised turbulence methods [1]

One commonly-used method for generating turbulent inlets is to try to synthesise them according to particular constraints. At the simplest level this can involve introducing a white-noise random component to the inlet velocity, with an amplitude determined by the turbulent intensity level. The white noise possesses no spatial or temporal coherence whatsoever – and so it is instantly destroyed by the Navier–Stokes solver. In Fourier techniques, the turbulent fluctuations are represented by a linear sum of sine and cosine functions, with coefficients representing the energy contained in each mode. In Principal orthogonal decomposition (POD) analysis, an ensemble of instantaneous realisations or snapshots is taken as input and basis functions optimal for the representation of the data are extracted. In other synthesis approaches, entirely random number data are generated which can then be processed using digital filters to generate the desired statistical properties such as spatial and temporal correlation.

3.3.2   Synthesized fluctuations in vortex method [1, 2]

This method is based on a superposition of coherent eddies where each eddy is described by a shape function that is localized in space. The eddies are generated randomly in the inflow plane and then convected through it. The method is able to reproduce characteristic length and time scales, first and second-order statistics as well as two-point correlations.

Divergence-free synthetic eddy method (DFSEM) proposed by Poletto et al. (2013) [65] to reduce near-inlet pressure fluctuations and the development length in the original SEM method by [66]. The steps in are the following:

1. User selection of inlet surface Ω

2. User definition of average velocity $\boldsymbol{u}(\boldsymbol{x})$, Reynolds stresses and turbulence length-scales $\sigma(\boldsymbol{x})$, for $\boldsymbol{x} \subset \Omega$

3. Eddy bounding box taken as: $\max\{x + \sigma\}$, $\min\{x - \sigma\}$ for $\boldsymbol{x} \subset \Omega$

4. Definition of the number of eddies

5. Assigning random positions $\boldsymbol{x}^k$ and intensities α^k to all the eddies

6. Eddies being convected through the eddy box, $\boldsymbol{x}^k = \boldsymbol{x}^k + \boldsymbol{U}_b * \Delta t$, where $\boldsymbol{U}_b = \int_\Omega \boldsymbol{u} ds / \int_\Omega ds$ is the bulk velocity

7. $\boldsymbol{u}'(\boldsymbol{x})$ calculated and superimposed to $\boldsymbol{u}$ to generate the inlet condition

8. Repeat steps 6-7 for all the subsequent time steps

The fluctuating velocity field is:

$$\boldsymbol{u}'(\boldsymbol{x}) = \sqrt{\frac{1}{N} \sum_{k=1}^{N} \frac{q_\sigma(|\boldsymbol{r}^k|)}{|\boldsymbol{r}^k|}} \times \alpha^k \tag{3.34}$$

where:

- N: the number of eddies introduced into the DFSEM

- $\boldsymbol{r}^k = \frac{\boldsymbol{x} - \boldsymbol{x}^k}{\sigma^k}$ with σ^k being eddy length scale for the kth eddy

- $q_\sigma(|\boldsymbol{r}|^k)$ is a suitable shape function

- α_i^k are random numbers with zero averages which represent eddy intensity

The fluctuating velocity field, taking into account the turbulence anisotropy, is:

$$u'_\beta(\boldsymbol{x}) = \sqrt{\frac{1}{N} \sum_{k=1}^{N} \sigma_\beta^k \left[1 - (d^k)^2\right] \epsilon_{\beta jl} r_j^k \alpha_l^k} \tag{3.35}$$

where:

- $d^k = \sqrt{(r_j^k)^2}$

- $\epsilon_{\beta jl}$ is the Levi-Civita symbol

The expression for the Reynolds stresses is also expressed as follows:

$$\langle u'_\beta u'_\gamma \rangle = \frac{1}{N} \sum_{k=1}^{N} \sigma_\beta^k \sigma_\gamma^k \epsilon_{\beta jl} \epsilon_{\gamma mn} \left\langle \left\{ \left[1 - (d^k)^2 \right]^2 r_j^k r_m^k \right\} \right\rangle \langle (\alpha_l^k)(\alpha_n^k) \rangle \tag{3.36}$$

Therefore σ_β^k and σ_γ^k are the eddy length scales for the kth eddy in β and γ directions.

This method in comparison with original SEM methods is able to provide a divergence-free velocity filed and also to reproduce all possible state of Reynolds stress anisotropy as a function of the characteristic ellipsoid eddy shapes described by the aspect ratio $\Gamma = \frac{\sigma_x}{\sigma_y} = \frac{\sigma_x}{\sigma_z}$.

3.3.3 Precursor simulation methods [1]

Other methods for generating inflow conditions involve running a separate, precursor, calculation of an equilibrium flow to generate a 'library' of turbulent data which can be introduced into the main computation at the inlet. In this method, since the inflow conditions for the main computation are taken from a genuine simulation of turbulence, they possess many of the required characteristics for the LES inlet conditions, including temporal and spatial fluctuation with correlation and a correct energy spectrum. The library itself can be generated in a number of ways, for example using periodic boxes of turbulence or cyclic channel flow calculations in which either periodic boundary conditions can be used, or recycling arguments can be invoked. Then, the velocity field in one plane normal to the streamwise direction is stored at each time step. The sequence of planes is then read in as inflow data for a separate calculation of the flow of interest.

The advantage of synthetic methods is the easy specification of turbulence parameters, such as length scales or turbulent energy levels as well as quick setup and modifications. The disadvantage is that they are inherently inaccurate. They also require an inlet section for development of random fluctuations into true turbulence. Despite this, precursor simulation methods generate true turbulence and so are inherently more accurate. The limitation of these methods is the difficulty of modification to generate the required state of turbulence. Using a mapping method to merge the auxiliary calculation into the main domain and also using sophisticated feedback control techniques to drive the flow towards a desired state, however, does make these techniques usable for LES simulations [1].

3.4 Evaluation of resolution in LES

LES and hybrid RANS-LES approaches are extensively being used for the prediction of the behavior of complex industrial cases. Often the cases include complex flow phenomena that

have not been examined before and for which the required grid resolution is not clear. There is then the risk that LES be performed on too coarse grid, leading to unreliable results. On the other hand, verification studies in LES are very challenging, since both errors in numerical discretization and also subgrid-scale-model are both influenced by grid resolution. Due to the significant computing times required, it is difficult to undertake systematic grid-dependence studies.

Several approaches are presented in the literature to evaluate the resolution of LES. Following Gant (2010) [67] and Celik (2006) [68], some of these methods can be used by a prior RANS simulation or one LES calculation. Therefore, they can also be called a single-grid estimators, which means that by running one LES calculation, they can be estimated. The multi-grid estimator methods require a number of LES calculations and some sort of Richardson Extrapolation.

3.4.1 Single-grid estimators

These methods or criteria include:

- The ratio between viscous and modelled turbulent viscosity $\nu/\langle\nu_r\rangle$:
  This is the simplest single-grid estimator. This quantity does not say much about how good the LES resolution is. It tells us how close the LES is to a DNS. In [69], Celik proposed that ν_r is replaced by ν_{eff} which is the sum of SGS and numerical viscosity which can be approximated as twice the SGS viscosity. This ratio is recommended to be between 5 and 20 depending on turbulent Reynolds number (300 and 1200). This ratio can be tested by itself and also it will be used for the calculation of the LES index of quality (see below). In a hybrid LES-RANS study of the channel flow at Reynolds number of 4000 by Davidson (2009) [70], this value is plotted for several cross sections of the channel and has the maximum value of 40.

- The ratio between modeled and resolved shear stress $\langle\tau_{12}^r\rangle/\langle u'v'\rangle$ [70,71]:
  This ratio behaves consistently with ratio between modelled and physical viscosity $\langle\nu_r\rangle/\nu$, which means that they both decrease upon grid refinement. They both have been tested by Davidson (2011) [71] for the case of plane asymmetric diffuser and plotted at different cross sections of the diffuser. However, it was shown that $\langle\nu_r\rangle/\nu$ has larger values in separated flow regions, which indicates that turbulence is better resolved at these locations, which is not correct. Therefore, this quantity is not a reliable quantity for the estimation of LES resolution.

- The ratio between resolved and total turbulent kinetic energy $\gamma = \frac{k_{res}}{k_{res}+k^r}$, $k_{res} = \frac{1}{2}\langle u_i' u_i' \rangle$:

  Pope (2004) suggests that if this ratio is 0.8 or above, then the turbulence is well resolved by the LES [72]. This ratio is tested by Davidson (2011) [71] for several grids and it presents values larger than 85% for all grids. Therefore, this quantity does not seem to be such a good measure of the resolution.

- Autocovariance or two-point correlations:

  Correlation means the tendency of two values to change together, either in the same or opposite way. If we think of $u(x)$ as a component of the velocity along a line in statistically homogeneous turbulence, the autocovariance or two-point correlation in space is:

$$R(r) \equiv \langle u(x+r)u(x) \rangle \tag{3.37}$$

where r is the separation distance between two points. As the two points move closer to each other, R increases. If the points move further away, R will go to zero. $R(r)$ is often normalized by the root-mean-square of velocity. Integral length scale L_{int} can be computed from the autocovariance which is the integral of $R(r)$ over the separation distance r i.e.

$$L_{int} = \frac{1}{\langle u^2 \rangle} \int_0^\infty R(r)dr. \tag{3.38}$$

A schematic of the integral length scale and the autocovariance is shown in Figure 3.2. It is clear that the two point correlations go to zero for separation distances which are greater than integral length scale.

The two point correlations are calculated by Davidson (2009, 2011) [70, 71]. In this study the separation distance is varied with the grid resolution. The number of cells needed for the autocovariance to approach zero is verified, thereby checking the grid resolution. It is recommended that in a good LES, the integral length scale should cover 8-16 cells. In this study, it is reported that the energy spectra and the ratio of the resolved turbulent kinetic energy to the total one is not a good measure of LES resolution. Two-point correlations are suggested as the best measures for estimating LES resolution.

A good practice is also to obtain the integral length scale L_{int} from the prior RANS simulation as $L_{int} = \frac{k^{3/2}}{\epsilon}$ and therefore to estimate the initial grid resolution for LES
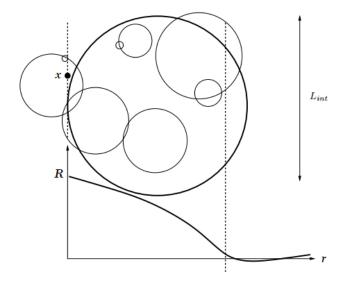
Figure 3.2 Schematic relation of autocovariance and integral length scale [5]

[70].

- It is advised that $(x^+, y^+, z^+) < (100, 2, 20)$ [67]:
  These quantities are wall units in the streamwise, normal and spanwise directions. These can also be initially estimated from the prior RANS simulations. Another criteria for the near wall grid resolution met by Davidson (2009) [70] is the ratio of the boundary-layer thickness, δ to Δx and Δz. Boundary layer thickness can be defined where ν_r/ν falls below one. In the mentioned study, the value for these ratios are maintained as $5 \leq \delta/\Delta x \leq 20$ and $100 \leq \delta/\Delta z \leq 400$.

- The ratio of the filter width to the Kolmogorov length scale $\eta = \left(\frac{\nu^3}{\epsilon}\right)^{1/4}$:
  This ratio should be less than 25, as stated by Celik (2005) [69]. The residual dissipation is $\epsilon^r = \tau_{ij}^r \overline{S}_{ij}$. The value for the Δ/η ratio can be calculated in an LES study and it is also used by Celik (2005) for the estimation of LES index of quality. The Kolmogorov length scale can also be estimated from a prior RANS simulation as a starting point for LES.

- The Subgrid Activity Parameter (s) by Geurts and Fröhlich (2002) $s = \frac{\langle \epsilon^r \rangle}{\langle \epsilon^r \rangle + \langle \epsilon_\mu \rangle}$:
  This is the ratio of the turbulent dissipation to the total dissipation, where the ϵ^r and ϵ_μ are the turbulent and molecular dissipations. The amount of turbulent dissipation is the central quantity used to assess the importance of the subgrid model, i.e., to quantify the amount of modeling in a LES compared to a DNS. By definition $0 \leq s < 1$ with $s = 0$ corresponding to DNS and $s = 1$ to LES at infinite Reynolds number [73].

- Examining the power spectrum for -5/3 slope of the Kolmogorov spectrum in the inertial subrange:

  The energy spectrum, defined as the Fourier transform of the autocovariance $R(\tau)$. For a variable ϕ:

$$E_\phi(w) = \frac{1}{2\pi} \int_{-\infty}^{\infty} R_\phi(\tau) e^{(-iw\tau)} d\tau \tag{3.39}$$

$E_\phi(w)$ is the power spectrum or power spectral density. With consideration of two-point, one time autocovariance, R_{ij}, the information in R_{ij} can be represented as a wave-number spectrum $\phi_{ij}(\bar{k})$. The directional information in $\phi_{ij}(\bar{k})$ can be removed by integrating over spherical shells of radius σ:

$$\int_0^{\infty} E(k) dk = \frac{1}{2} \int_0^{\infty} [\iint \phi_{ii}(\bar{k}) d\sigma] dk \tag{3.40}$$

Experimentally $R_{11}(r,0,0)$, longitudinal velocity correlation and $R_{22}(r,0,0)$, transverse velocity correlation and their Fourier transformation $F_{11}(k_1)$ and $F_{22}(k_2)$ are measured, and are called 1D longitudinal and transverse spectrum.

Kolmogorov's second similarity hypothesis states that in every turbulent flow at sufficiently high Reynolds number, the statistics of the motions of scale l in the range $l_0 \gg l \gg \eta$, where l_0 is the size of the largest eddies, have a universal form that is uniquely determined by ϵ, independent of ν. This hypothesis predicts that, in the inertial subrange, the energy-spectrum function is [16]:

$$E(\kappa) = C\epsilon^{\frac{2}{3}} \kappa^{\frac{-5}{3}} \tag{3.41}$$

Analyzing the Kolmogorov's energy spectrum thus can provide an indication on the quality of the LES.

- LES index of quality (LES_{IQ}):

  This index is proposed by Celik et al. (2005) as a single grid estimator [69] which can be based on the Kolmogorov scale, hence it is called the relative Kolmogorov scale index:

$$LES_{IQ_\eta} = \frac{1}{1 + 0.05\left[\frac{h}{\eta_{eff}}\right]^{0.3}} \tag{3.42}$$

here h is the grid size that can be the same as the filter width Δ. The relative SGS-viscosity index is also:

$$LES_{IQ_\nu} = \frac{1}{1 + 0.05\left[\frac{\langle \nu_{eff} \rangle}{\nu}\right]^{0.53}} \tag{3.43}$$

All the eff subscripts mean that ideally the effect of numerical dissipation should be included as for viscosity $\nu_{eff} = \nu^r + \nu_{num} + \nu$. The ν_{num} could be assumed to be proportional to residual viscosity. Good LES predictions are reported with LES_{IQ} of the order 80–95%.

3.4.2 Two- or multi-grid estimator

- Richardson extrapolation on the resolved turbulent kinetic energy proposed by Celik et al (2005) [69]:

$$LES_{IQ_k} = 1 - \frac{\mid k_{tot} - k_{res} \mid}{k_{tot}} \tag{3.44}$$

it is postulated that

$$k_{tot} - k_{res} = k_{eff_{SGS}} = \alpha_k h^p \tag{3.45}$$

where p is the order of the numerical scheme. There are three unknowns, and these can be determined from three calculations on significantly different but geometrically similar grids. If three grid calculations become too expansive, then one can use the theoretical order of the scheme; if that is not known, one can assume $p = 2$ [74]. These methods are applied to various test cases by Celik (2009) [74].

- Systematic grid and model variation by Klein (2005) [75]:
  This method involves running three LES calculations: a standard LES, a coarse-grid LES and an LES with the SGS model constant modified. The basic idea is, in addition to a grid variation, to change the model contribution as well. This method is applied for the isothermal, turbulent, plane jet and a turbulent channel flow.

As it was mentioned some of these criteria have been already assessed in literature. However, to the best of our knowledge, no comprehensive assessment has been done so far to thoroughly compare and evaluate them. The accuracy of some of these indicators for the grid assessment in LES will be verified in the present study. Another point to be considered is that some

of these criteria are limited by the choice of the SGS model, for example to calculate the residual dissipation we need the residual shear stress and the residual shear stress can be directly calculated in the dynamic model. Therefore in order to calculate this indicator we are restricted to use the dynamic model. To use the Smagorinsky model we need to calculate the strain tensor and residual viscosity and use the equation (3.14).

3.5   Discretization and Numerical Solution

CFD solvers often use the finite-volume method to convert a general scalar transport equation to an algebraic equation that can be solved numerically. The finite volume method is based upon dividing the computational domain into many small non-intersecting polyhedra called control volumes (CVs). When the variables are stored at the center of the control volumes, this method is called cell-based and the value at the centroid represents the value for the whole control volume. The discretized form of the equation can be obtained by integrating the original equations over a control volume and a time interval of Δt. To convert volume integrals to face integrals, Gauss theorem is used. The conservative form of the general scalar transport equation for the property ϕ takes the form:

$$\frac{\partial \phi}{\partial t} + \nabla.(\boldsymbol{u}\phi) = \nabla.(\Gamma\nabla\phi) \tag{3.46}$$

which is integrated to a 3-D control volume:

$$\int_V \frac{\partial \phi}{\partial t}dV + \int_V \nabla.(\boldsymbol{u}\phi)dV = \int_V \nabla.(\Gamma\nabla\phi)dV \tag{3.47}$$

By applying Gauss theorem:

$$\frac{\partial}{\partial t}\int_V \phi dV + \oint_S \phi\boldsymbol{u}.\boldsymbol{n}dS = \oint_S \Gamma\nabla(\phi).\boldsymbol{n}dS \tag{3.48}$$

This equation is discretized to produce a system of algebraic equations which can be solved numerically. The volume integrals are approximated as $\phi_P V_{CV}$ and the surface integrals are approximated as a sum over the faces of the control volume:

$$\oint_S \phi\boldsymbol{u}.\boldsymbol{n}dS \approx \sum_f (\boldsymbol{u}_f.\boldsymbol{n})S_f\phi_f, \tag{3.49}$$

$$\oint_S \Gamma\nabla(\phi).\boldsymbol{n}dS \approx \sum_f (\nabla_f\phi.\boldsymbol{n})S_f\Gamma_f \tag{3.50}$$

The index f in the above equations stands for the value in the centroid of the face.

The discretization process includes application of temporal and spatial schemes which are explained in the following section. More information about the OpenFOAM CFD code is provided in Annex A.

3.6   Temporal and spatial schemes

The choice of the temporal and spatial schemes should be a compromise between accuracy and stability. Implicit second-order backward time scheme is used which is conditionally stable. This scheme uses the value of the unknown at the current time step and the two preceding time steps:

$$\frac{\partial \phi}{\partial t} = \frac{1}{\Delta t}(\frac{3}{2}\phi - 2\phi^o + \frac{1}{2}\phi^{oo}) \tag{3.51}$$

where Δt is time step. For all the simulations time steps are chosen to be small enough to keep the Courant number below one to ensure the stability of the simulations.

Second-order linear scheme is used for the convection of the velocity. Convection of the subgrid scale turbulent kinetic energy is also calculated using a blend between first and second order methods.

Pressure-velocity coupling is done based on a method which is a blend of the transient SIMPLE (Semi-Implicit Method for Pressure-Linked Equations) and PISO (Pressure Implicit with Splitting of Operators) algorithms. In this algorithm, as in Figure 3.3, at the beginning of each time-step, the algorithm increases the current simulation time by the value of the time-step. Then the pressure-velocity coupling loop is executed. Inside the loop, the momentum equation is solved first, after which the corrector loop is entered. Inside the corrector loop, the pressure equation is solved and the velocity field is corrected ensuring that it is divergence free. Finally, all equations related to turbulence modelling are solved which for instance for the LES with k-equation SGS model will be Equation 3.19.

The Geometric agglomerated algebraic multigrid solver (GAMG) with combined DIC (Diagonal-based Incomplete Cholesky) and Gauss Seidel Smoother is used to solve pressure equations. Momentum and turbulence equations are solved using a smooth solver with symmetric Gauss Seidel Smoother. The smooth solver in OpenFOAM uses Lower-Upper decomposition methods.
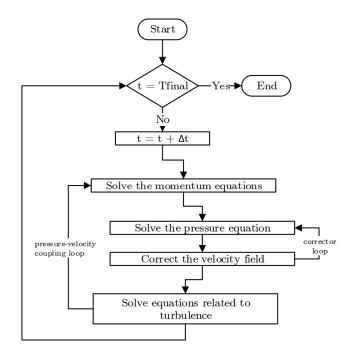
Figure 3.3 Steps in pressure-velocity coupling

CHAPTER 4   VERIFICATION AND VALIDATION

As it was mentioned earlier, the main focus of this research is on the evaluation of the mesh resolution for the large-eddy simulations of internal incompressible flows which resemble those inside hydraulic turbine draft tubes. This objective is inline with the verification and validation of the OpenFOAM CFD code. Within the LES framework there are certain parameters such as inlet boundary condition, SGS models and the mesh resolution which require full understanding and evaluation. With verification, we determine if our simulations accurately represent the conceptual models. While the validation is determining if the simulations represent the real world [76]. Word-by-word definitions for verification and validation are given in the AIAA guide [77]:

Verification: The process of determining that a model implementation accurately represents the developer's conceptual description of the model and the solution to the model.

Validation: The process of determining the degree to which a model is an accurate representation of the real world from the perspective of the intended uses of the model.

In order to fulfill the objectives of this research and to perform the verification and validation study in this research, as it was mentioned earlier, instead of proceeding to the application of LES to real test cases of hydraulic turbine draft tube, two academic test cases are considered. The first case is a turbulent flow in a channel and the second is the flow through an abrupt expansion. The reason to choose the first case is that this case is an internal flow with a simple geometry for which DNS data is available and the LES results and framework will be verified and validated using the available data. The second test case, an abrupt expansion, closely represents the flow inside a hydraulic turbine draft tube at part load operating condition. The experimental data for this case is also available at several swirl and Reynolds numbers which will be used for the validation of LES results.

For the case of turbulent channel flow, two verification studies are performed which include verification of the size of inlet eddies and verification of mesh resolution. In each of these studies, the objective of the study, the method of evaluation, the hypothesis and expectation criteria are identified and explained. Moreover, a validation study is also performed to evaluate the accuracy of several SGS models in LES. For the sudden expansion case also, a verification analysis of the mesh resolution is performed and the results of RANS and LES are compared and validated against the experimental data.

In the following sections, first a description of each case including physical and geometric

modelling is provided. Then a summary of the boundary conditions and solver setups is presented. Afterwards, details for each verification and validation case is included in each subsection, followed by results of the studies. The mentioned structure is maintained for each case of the channel flow and sudden expansion.

4.1 Turbulent channel flow case description

Channel flow is a classical model problem for the investigation of wall-bounded turbulence. The purpose of this section is to provide detailed information concerning grid requirements and other computational setups to use LES for solving the turbulent flow for problems where turbulent boundary layers play an important role. This case is also chosen as it is a very well documented test case with wall-bounded turbulence, and we use DNS data to validate LES results.

The turbulent flow in the channel is simulated at a moderate Reynolds number. The geometry of the channel is shown in Figure 4.1. The flow in the channel is considered statistically homogeneous in the spanwise direction (z) and statistically developing in the streamwise (x) and channel-height (y) directions. Domain size for the channel is $(20\pi, 2, \pi)$ [m]. The physical modelling is done based on friction Reynolds number which is $Re_{u_\tau} = \frac{u_\tau \delta}{\nu} = 395$, where $\delta = 1$ [m] is a characteristic length (Channel half-height) and friction velocity, $u_\tau = \sqrt{\frac{\tau_w}{\rho}}$ is assumed to be equal to 1 $\left[\frac{m}{s}\right]$. This assumption should be validated. Kinematic viscosity of the fluid is $\nu = 0.002532$ $\left[\frac{m^2}{s}\right]$ and the flow bulk velocity is $\boldsymbol{U}_{bulk} = (17.55, 0, 0)$ $\left[\frac{m}{s}\right]$. `blockMesh` which is a structured hexahedral mesh generator is used for the domain discretization due to its simple geometry. An example of `blockMeshDict` is provided in appendix in Section A.2. The initial number of nodes for the mesh was chosen as (500, 46, 82) with a total of 1,866,000 cells. Therefore the wall units which are the normalized distance of the first mesh next to the wall are $(x^+, y^+, z^+) = (49.36, 1.1, 15.1)$.

4.2 Boundary conditions and computational setup of channel flow

A summary of the computational setups for LES analysis of the channel flow is given in Appendix in Section A.1. Regarding the boundary conditions, two sets of boundary conditions are considered for the generation of the inflow turbulence. Firstly, periodic boundary conditions are used between the inlet and outlet. The LES calculations with periodic boundary conditions is performed as a reference solution to compare with the results of the DFSEM approach. Then secondly, the divergence-free synthetic eddy method (DFSEM) of Poletto et al. (2013) [65] is used to generate inlet turbulence for which the details of the method
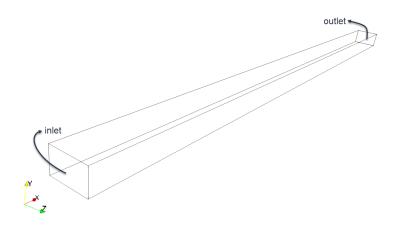
Figure 4.1 The geometry of the channel

are provided in Subsection 3.3.2. The results of these two methods are compared with each other and validated against the DNS data [78]. The boundaries in the spanwise direction are considered periodic. The OpenFOAM term for periodic boundary condition is `cyclic`. The other two boundaries represents walls which induce no-slip boundary conditions for velocity. A summary of the OpenFOAM boundary conditions for these two cases are presented in Tables 4.1 and 4.2 for periodic and DFSEM boundary inlet conditions respectively. In these tables, the value for `internalField` implies the values considered for the initialization of the field.

Table 4.1 OpenFOAM boundary condition for the channel flow (Periodic)

Variable	internalField	inlet	outlet	sides	walls
k $\left[\frac{m^2}{s^2}\right]$	0	cyclic	cyclic	cyclic	fixedValue (0)
U $\left[\frac{m}{s}\right]$	17.55	cyclic	cyclic	cyclic	noSlip
p $\left[\frac{m^2}{s^2}\right]$	0	cyclic	cyclic	cyclic	zeroGradient
ν_t $\left[\frac{m^2}{s}\right]$	0	cyclic	cyclic	cyclic	zeroGradient

As within the Tables 4.1 and 4.2, the `fixedValue` boundary condition in OpenFOAM is a Dirichlet boundary condition. For this boundary condition, face values are set according to the assigned reference value:

$$\phi_f = \phi_{ref} \tag{4.1}$$

A `zeroGradient` boundary condition which is a wrapper around the fixed gradient (`fixedGradient`), is a Neumann boundary condition that is implicit and implies fixed normal-gradient. For this boundary condition, face values are evaluated according to:

Table 4.2 OpenFOAM boundary condition for the channel flow (DFSEM)

Var	internalField	inlet	outlet	sides	walls
k $\left[\frac{m^2}{s^2}\right]$	1×10^{-5}	fixedValue (internalField)	fixedValue (internalField)	cyclic	fixedValue (0)
U $\left[\frac{m}{s}\right]$	17.55	turbulentDFSEMInlet R, L, U from DNS delta (2) nCellPerEddy (1) mapMethod (nearestCell) value (internalField)	inletOutlet inletValue (0 0 0) value (0 0 0)	cyclic	noSlip
p $\left[\frac{m^2}{s^2}\right]$	0	zeroGradient	fixedValue (0)	cyclic	zeroGradient
ν_t $\left[\frac{m^2}{s}\right]$	0	calculated (1×10^{-8})	calculated (1×10^{-8})	cyclic	zeroGradient

$$\phi_f = \phi_c + d\nabla\phi_{ref} \tag{4.2}$$

where ϕ_c is cell value, $\nabla\phi_{ref}$ is reference gradient and d is face-to-cell distance.

The OpenFOAM `inletOutlet` condition is a wrapper around a mixed condition, which is a Robin boundary condition and is a linear blend of fixed value and gradient conditions. This condition sets the patch value to a user-specified fixed value for reverse flow, in the present case ϕ_{ref}.

The boundary condition which is specified as `calculated` is the boundary condition which is not designed to be evaluated; it is assumed that the value is assigned via field assignment. The specified value is an optional value entry. As we can see in Table 4.2, it seems that ν_t is considered as an auxiliary variable in OpenFOAM for turbulent flow simulations. Therefore after solving the main equations and turbulence equations, the value for ν_t, based on the chosen SGS model, will be calculated form one of the Equations 3.15, 3.17 or 3.20.

The details about the DFSEM boundary condition implementation in OpenFOAM is provided in Table 4.2. As it was explained earlier, `turbulentDFSEMInlet` is an inflow turbulence generator which generates turbulent eddies that are continuously evolving across an inlet patch, based on the Reynolds stresses (R), velocity profile (U) and eddy length scales (L). The eddies are injected to generate coherent flow structures that persist into the domain, aiding the process of establishing a fully developed turbulent flow. In the simulations performed for the channel flow, the profiles for R, U and L are provided from the DNS of Moser et al. (1999) [78].

In Table 4.2, `delta` value in the row of boundary condition for U, represents a domain-based length scale, e.g. the overall channel height. The DFSEM approach uses the length scale entry (L) in order to set the length of the eddy along its principle axis which is the streamwise direction here. The eddy scales in the remaining 2 dimensions are set by the model in order to form elliptical shapes. The eddy length scale is limited to be larger than the mesh cell scale; however, eddies at the scale of 1 cell tend to dissipate quickly and their influence (in terms of structure) is not transported into the domain. In practice, setting the scale to 3 to 5 times the mesh scale is sufficient to produce flow structures that persist throughout the domain. This set-up is accommodated by setting the optional entry for `nCellsPerEddy`. The influence of this entry is further elaborated in the current research. `mapMethod` is the method to map reference values which uses the values at the nearest cells (`nearestCell`).

Referring to the original DFSEM method presented in Subsection 3.3.2, therefore it can be interpreted that the N value which is controlling the number of eddies in the original method, in the OpenFOAM implementation is assigned as number of cells per eddy (`nCellsPerEddy`). Moreover, the value for Ω, being the inlet surface selected by user, is considered as channel height with the parameter δ. The eddy length scales, σ in the original method, is assigned as L in OpenFOAM.

4.3 Verification of the inlet eddy sizes in channel flow

The first verification analysis, as explained earlier in this chapter, is performed for the size of inlet eddies in the channel flow case. This verification analysis is performed firstly for the mean velocity field and Reynolds stress field. Secondly, the verification analysis of the inlet eddy sizes is performed directly for the fluctuating velocity field at a point in the domain. The details of these verification analysis are provided in the following sections.

4.3.1 Verification of the inlet eddy sizes in channel flow for mean velocity and Reynolds stress field

Table 4.3 summarizes the objective, method of evaluation, hypothesis and the expected criteria for this verification study. In this verification study, we want to investigate the influence of the inlet eddy sizes on the development of the flow inside the channel and we want to verify that we can obtain the mean velocity and Reynolds stress field independent of the size of eddies generated at the inlet and transported into the domain. Therefore, the effect of the size of the inlet eddies will be evaluated based on the development length of the mean streamwise velocity profile inside the channel. Our hypothesis is that, further increment in

the size of the inlet eddies will not further exhibit changes in the flow development length. Starting the simulation by considering 1 cell per eddy simulation, and then increasing to 3 and 5, we expect that simulating each eddy with an adequate number of 3 cells would allow capturing non-decaying turbulence fluctuations in the domain.

Table 4.3 Details of the first verification test for the inlet eddy sizes

Objective	Method of evaluation	Hypothesis	Expectation criteria
To verify that the mean velocity and Reynolds stress fields are independent from the generated turbulence at the inlet	Development length of the flow	Independence of the development length from the increment in the size of inlet eddies for a given mesh	Adequacy of minimum number of 3 cells for defining the inlet eddies

The results of this verification study is provided in Figure 4.2 and Figure 4.3. In these figures, the downstream development of the profiles of the mean streamwise velocity and $\langle u'u' \rangle$ component of the Reynolds stress is presented respectively for several cross sections and for different values of the parameter `nCellsPerEddy` representing the eddy sizes at the inlet. Moreover, the results for the periodic boundary condition case is also provided in the same figure as a reference for the comparison.

The results of these simulations show enormous changes in the profiles of the mean streamwise velocity and $\langle u'u' \rangle$ component of the Reynolds stress, which are shown in Figure 4.2 and Figure 4.3. In these figures we can see how the flow develops across the channel using different conditions for the inlet eddies. Changing the value of the number of mesh cells per eddy to a value of 3, which means that each eddy is represented by at least 3 mesh cells in the domain, although requiring smaller time steps, improves the results of the development of the flow in the channel. The influence of increasing further this value to 5, does not exhibit a further improvement in the flow characteristics and only imposes more expensive computations in terms of time steps. In the aforementioned figures the results at each streamwise section is averaged in the spanwise direction and time, therefore the notation $\langle \rangle$ and $\{YZ\}$ index in the axis titles imply averaging in time and in the $\{YZ\}$ plane respectively.

In Figure 4.3, the cross sections with the values of $x/\delta = 0.06$ and $x/\delta = 62.7$ represent the center of the first cell immediately after and before the inlet and outlet boundaries. It seems that a minimum number of cells in the streamwise direction and away from the boundaries is required for the attenuation of the effect of boundary conditions. Moreover,

(a) 1 cell Per Eddy

(b) 3 cells Per Eddy
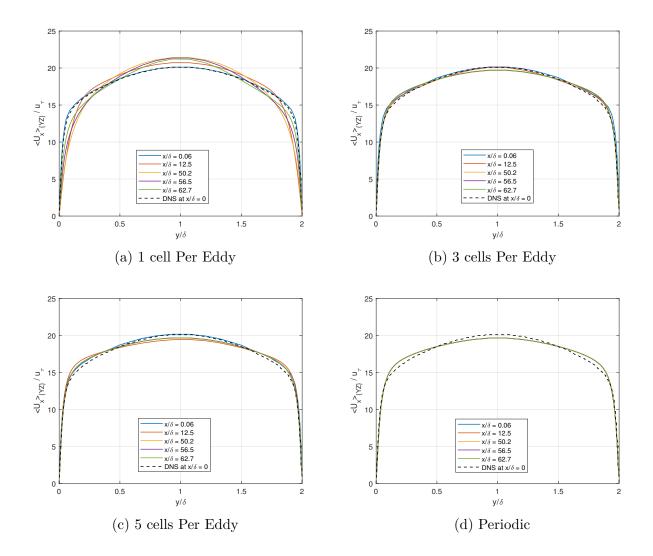
(c) 5 cells Per Eddy

(d) Periodic

Figure 4.2 Mean velocity profiles at selected streamwise locations using various inlet conditions

it seems that although both boundary conditions with 3 and 5 mesh cells are representing shorter development length in comparison with the one with one mesh cell per eddy, which is evident by the results at downstream locations of x/δ of 12.5, 50.2 and 56.5 being almost on top of each other, but the results of the 5 cells per eddy is worse than with 3 cells per eddy. A possible explanation could be that there should be an optimum number of cells per eddies for a given mesh, and increasing this value does not necessarily provide more accurate results. In other words the optimum value for this parameter could be mesh dependent. This hypothesis needs further investigation and analysis which is beyond the scope of this research.

The same comparison is also drawn for the results of the root-mean square of the streamwise

(a) 1 cell Per Eddy

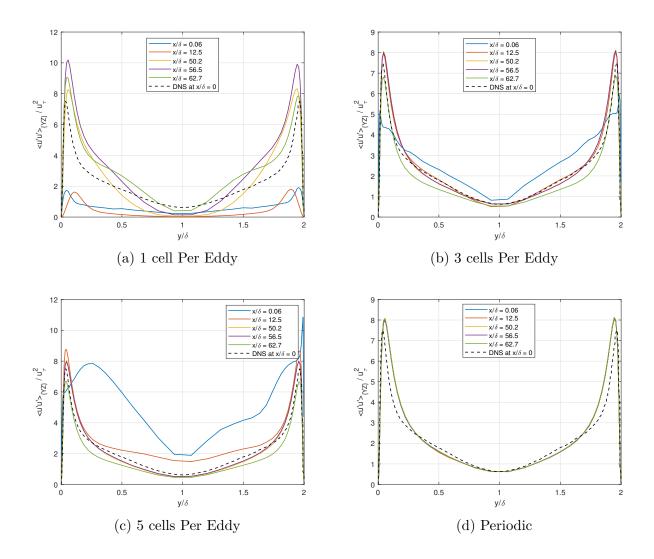(b) 3 cells Per Eddy

(c) 5 cells Per Eddy

(d) Periodic

Figure 4.3 $\langle u'u' \rangle$ profiles at selected streamwise locations using various inlet conditions

velocity fluctuations and mean streamwise velocity which are also averaged across the channel direction in Figure 4.4. The results clearly show the improvement of the results obtained by increasing the value for `nCellsPerEddy` and the rapid convergence of the profiles towards the fully-developed one with a short recovery length.

4.3.2 Verification of the inlet eddy sizes in channel flow for a fluctuating velocity field

The second part of this study presents verification results of the velocity fluctuations in the flow. The details of this study are summarized in Table 4.4. The objective of this analysis is to further investigate the effect of the size of the inlet eddies on the downstream fluctuating

(a) RMS of streamwise velocity fluctuations   (b) Mean streamwise velocity
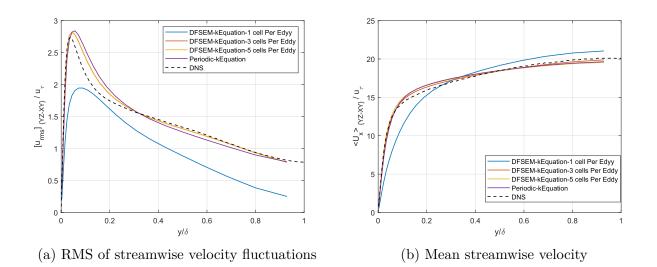
Figure 4.4 Comparison of velocity profiles for different inlet conditions

velocity field. For this reason, time variation of the instantaneous velocity is captured at a point at the center of the domain where $(x/\delta, y/\delta, z/\delta) = (10\pi, 1, \pi/2)$. Our hypothesis is that the amplitude of the downstream fluctuations should be independent of the generated turbulence at the inlet in terms of the size of the eddies, and again definition of each eddy by a sufficient number of mesh cells should allow converging to the level of fluctuations in the periodic field.

Table 4.4 Details of the second verification test for the inlet eddy sizes

Objective	Method of evaluation	Hypothesis	Expectation criteria
To verify that the level of turbulence in the flow is independent from the generated turbulence at the inlet	Time variation of instantaneous velocity field at a point	Independence of the amplitude of the fluctuations from the increment in the size of inlet eddies for the same mesh	Adequacy of fixed number of cells for defining the inlet eddies and convergence of the level of fluctuations in the flow to the one in the periodic field

The results of this verification analysis are presented in Figure 4.5. In this figure, the results of the instantaneous velocity for 1 and 3 mesh cells per eddy are presented, which clearly show

the lower level of fluctuations when defining each eddy with one mesh cell, in comparison with 3 cells per eddy. A further increment to 5 cells per eddy does not exhibit bigger fluctuations in the flow, which already converged to the fluctuating field in the periodic case for 3 cells per eddy.
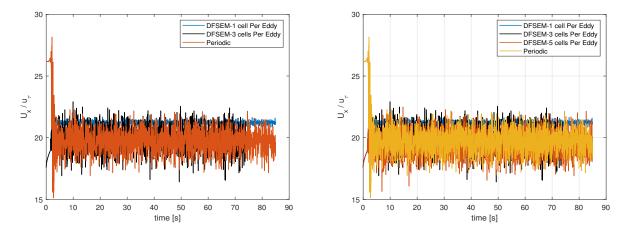

Figure 4.5 Variation of instantaneous velocity at center of the domain where $(x/\delta, y/\delta, z/\delta) = (10\pi, 1, \pi/2)$ with time

4.4   Validation of the SGS models in LES of channel flow

All simulations so far were performed using k-equation as the SGS model. A validation study of the three SGS models is performed. This validation study is important to investigate the performance of the SGS models in LES calculations. The details of this validation study are summarized in Table 4.5. In this study, the results of the mean and RMS velocity and shear stress are validated against DNS data. We expect that more complicated models such as the k-equation model show better performance.

Table 4.5 Details of the validation study for the SGS models

Objective	Method of evaluation	Hypothesis	Expectation criteria
To validate the accuracy of SGS models for space-averaged mean and RMS of velocity and shear stress field	Validation against analytic and DNS profiles	Improvement of the results using more advanced models	Expect to better match DNS data with more advanced models

Simulation results for the different SGS models including WALE, Smagorinsky and k-equation are calculated and compared to each other and to DNS data in Figure 4.6. We also draw this comparison against the analytical profile of the mean velocity in the same figure. The results generally show inferior accuracy of the Smagorinsky model in comparison with the WALE and k-equation models. The k-equation model shows slightly better results, closer to DNS data and the analytical profile, while the WALE model requires less computational time.

Figure 4.6 Comparison of mean velocity profiles for different SGS models

LES results for components of the root-mean square of velocity fluctuations using various SGS models are also presented in Figure 4.7. The results of the k-equation and WALE models show better agreement with DNS data in general and we still observe some inferior results of the Smagorinsky model. The WALE model overpredicts the value for u_{rms} near the wall and the results for v_{rms} with both the WALE and k-equation models are very close. The w_{rms} component shows slightly better performance for the WALE model in comparison with the k-equation near the wall and the peak value is also closer the the DNS data for the WALE model. We observe the same behavior for shear stress profile, $-\langle uv \rangle$.
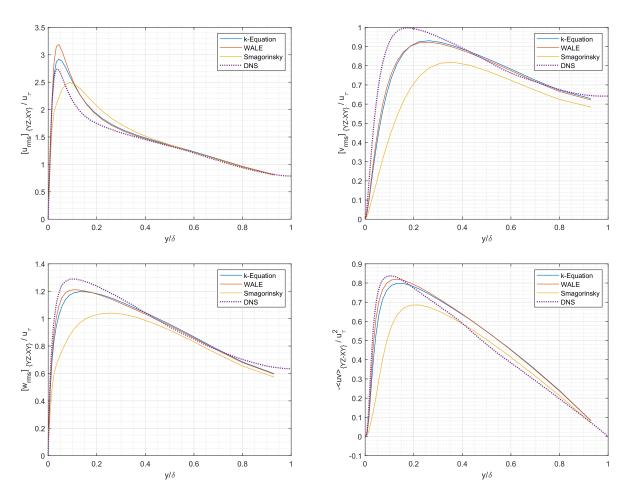
Figure 4.7 Comparison of RMS of velocity fluctuations for different SGS models

4.5 Verification of the mesh resolution in channel flow

This section is dedicated to the verification of the influence of the mesh resolution on LES results inside the channel. As mentioned earlier, the verification analysis for the LES is quite challenging since errors in both numerical discretization and sub-grid models are both influenced by the mesh resolution. Within this verification analysis, we are trying to evaluate the effect of the mesh resolution on various LES results and indicators. To this aim, three different verification studies are performed relating to mesh resolution. For this analysis, two other meshes are generated. The details of these meshes are presented in Table 4.6. In this table, the values for the wall units in the three directions are presented and are within the ranges presented in Chapter 2. The finer meshes require smaller time steps to ensure the stability and convergence of the simulations. The time steps used and the value obtained for the friction velocity as a criteria for the validation of the results versus DNS data are given in Table 4.7. This value is averaged over the entire wall. This value is calculated as follows:

$$u_\tau = \sqrt{\frac{\tau_w}{\rho}} \tag{4.3}$$

$$\tau_{wall} = \rho \nu_{eff} \frac{\partial \bar{U}}{\partial y}\bigg|_{y=0} \tag{4.4}$$

Table 4.6 Details of the numerical grids

Name	Number of cells	Total size	Δx^+	Δz^+	y^+
Mesh 1	$397 \times 38 \times 65$	980590	62.51	19.09	1.34
Mesh 2	$500 \times 46 \times 82$	1886000	49.63	15.13	1.11
Mesh 3	$630 \times 58 \times 103$	3763620	39.39	12.05	0.91

Table 4.7 Designated time step and results of friction velocity

Name	Time step	$u_\tau [m/s]$
Mesh 1	0.002	0.94
Mesh 2	0.002	0.96
Mesh 3	0.001	0.98

The following sections cover the results of the three verification analysis performed for the channel flow. First, the effect of the mesh resolution on the mean and RMS velocity is investigated. Second, the verification analysis is performed for the two-points autocorreleation of the velocity fluctuations in the domain. Third, the verification analysis is performed for the results of the energy spectra.

4.5.1 Mean velocity and RMS of velocity fluctuations results

A summary of the details of the first verification study for the mesh resolution is presented in Table 4.8. This verification study focuses on the effect of the mesh resolution on the mean and RMS velocity and shear stress field. In this analysis, we expect to get converging profiles with refinement in the meshes and results which are independent from further mesh refinement.

Table 4.8 Details of the first verification test for the mesh resolution

Objective	Method of evaluation	Hypothesis	Expectation criteria
To verify the influence of the mesh resolution on space-averaged mean and RMS velocity and shear stress field for the chosen SGS model	Asymptotic converging behavior of the profiles	Independence of the profiles from further mesh refinement	Asymptotic convergence of the profiles to analytical and DNS profiles

The results of the aforementioned verification analysis for the three mesh resolutions including components of mean velocity and RMS of velocity fluctuations are presented in Figures 4.8 and 4.9. The results show different flow behavior when moving farther from the wall in the outer layer ($y^+ > 50$). The finest mesh gives results that are in very good agreement with DNS across the whole region. We can conclude that grid refinement has a positive effect which is reflected in the gradual increase in the accuracy of the obtained results. The results of the RMS of velocity fluctuations show that all three components converge towards the DNS data as the mesh gets refined. Closer to the core region of the channel ($y/\delta > 0.5$), mesh 2 shows generally better prediction for three components of RMS of velocities.

It can be shown analytically that for channel flow, the profile of the total shear stress which is the sum of the viscous and turbulent shear stresses varies linearly across the channel. However, viscous stresses play a significant role only in the viscous wall region where $y^+ < 50$ and therefore, outside that region, the profile of the turbulent shear stress alone can be expected to vary linearly. The profiles of the computed turbulent shear stress in Figure 4.9 presents good agreement with the aforementioned theoretical analysis. The finest mesh results shows the best agreement with DNS.
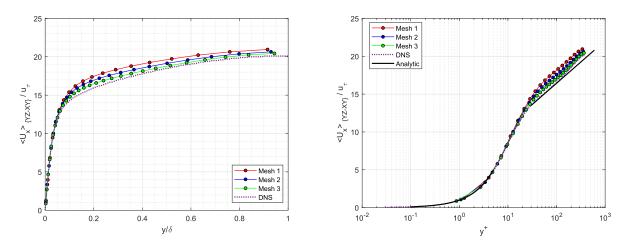
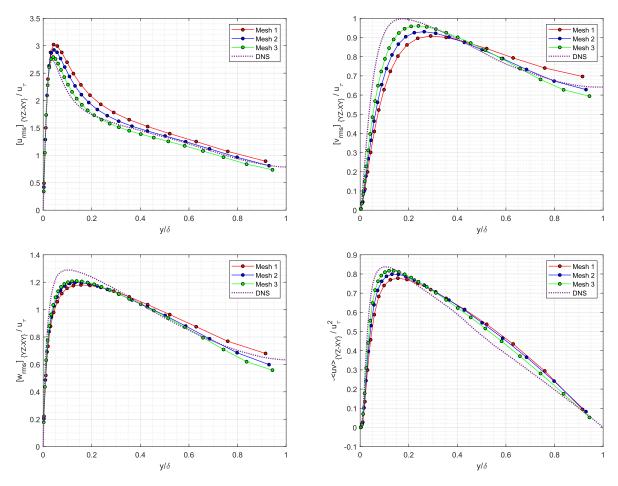Figure 4.8 Comparison of mean velocity profiles for different mesh resolutions

Figure 4.9 Comparison of RMS of velocity fluctuations for different mesh resolutions

4.5.2 Two-point autocorrelation results

The second verification study for the mesh resolution is done for the two-point autocorrelation of velocity fluctuations. The details of this study are presented in Table 4.9. The objective of this verification analysis is to evaluate the influence of the mesh resolution on the profiles of the two-point auto-correlation of velocity fluctuations. Additionally, two-point autocorrelations can be used to evaluate the adequacy of the chosen size of the computational domain. The domain is considered large enough, if the two-point correlations become negligibly small compared to the length scale of the domain, in each spatial direction.

Table 4.9 Details of the second verification test for the mesh resolution

Objective	Method of evaluation	Hypothesis	Expectation criteria
To verify the influence of the mesh resolution on spatial autocorrelation of fluctuations of the velocity for the chosen SGS model	Calculation of integral length scales	Independence of the integral length scales from the mesh resolution and mesh convergence	Adequacy of a sufficient number of cells to recover integral length scales

The results for the two-point autocorrelation of components of velocity fluctuations at two y^+ values for x and z spatial directions are calculated and compared versus DNS data and also to the results for the reference solution computed with periodic boundary conditions. Positions in the flow for y^+ values of around 5 and 150 are chosen for this comparison, in order to be near and quite far from the wall. The results at these distances from the wall are presented in Figure 4.10 and 4.11 respectively. In each figure, in the left column we see the results along the x-direction and in the right column along the z-direction. From top to bottom we can also see the results for the components uu, vv and ww.

In general, the profiles indicate that the chosen size of the domain is large enough to accommodate all the relevant turbulent structures, since the profiles reach near zero value or an asymptotic value in each computed direction. These profiles show higher sensitivity of this indicator to the mesh resolution, especially in the x-direction. The results computed with DFSEM boundary conditions, overall, show better performance than the periodic case, almost for all the cases, even for the coarsest mesh.

The calculated values for the integral length scales from Equation 3.38 using the profiles of the autocorrelation of velocity fluctuations are also presented in Table 4.10 and, for each

value, the number of cells covering that length is presented in Table 4.11. Since the mesh is uniform in the x and z directions, the value obtained for the integral length scale in each direction is divided by the cell size in the corresponding direction to get the number of cells covered by the integral length scales and to compare these value with the criteria of adequacy of 8-16 cells to recover integral length scales.

In the results in the Table 4.10 we do not observe a consistent trend in the results. In some cases the results have a decreasing behavior with mesh refinement as it is the case for L_x calculated at $y^+ = 150$ with all the components. However at $y^+ = 5$, we see the decreasing and then increasing trend in the results. These behaviors in the results show that further mesh refinement is still required to get a converged value for the integral length scales, especially in the streamwise direction, since the difference in the results for Mesh 3 and 2 is still big.

In addition, it is important to be in convergence zone for the results of the mesh refinement and then calculate the number of cells covered by the integral length scales. Therefore it makes more sense to compare the number of cells for the mesh-converged and mesh-independent values of integral length scales. Moreover, it seems that the values for the integral length scale in the z-direction is less sensitive to the mesh resolution and although the values for L_z are close to the DNS values, the criteria of length scale being covered by the 8-16 cells is not much applicable here.
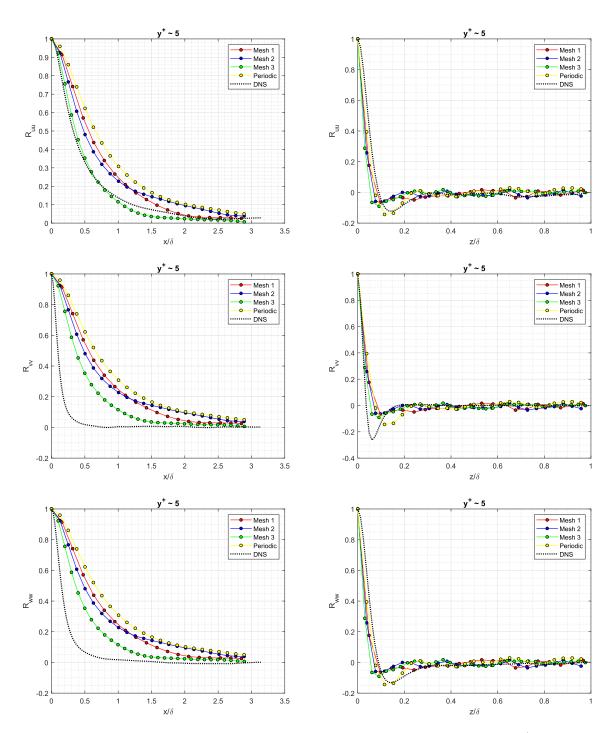
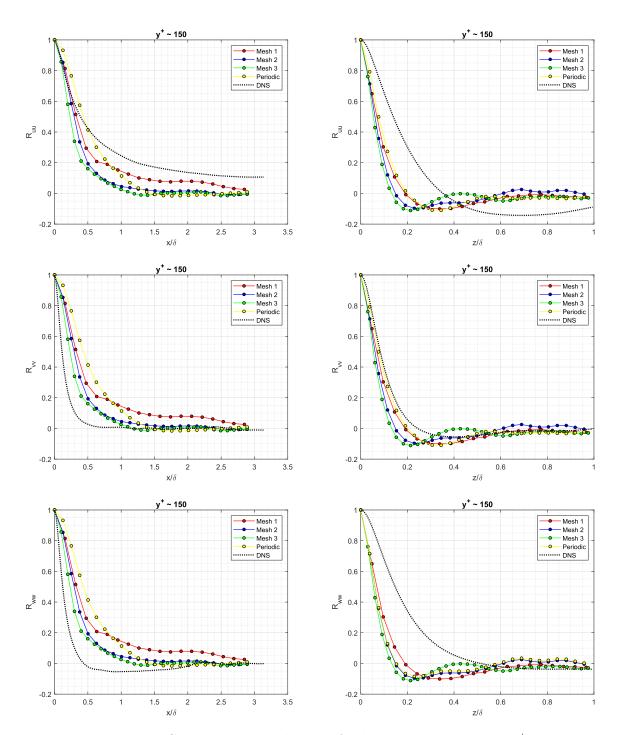Figure 4.10 Spatial autocorrelation of velocity components at $y^+ = 5$

Figure 4.11 Spatial autocorrelation of velocity components at $y^+ = 150$

Table 4.10 Integral length scales

	y^+	L_x					L_z				
		Mesh: 1	2	3	Periodic	DNS	Mesh: 1	2	3	Periodic	DNS
uu	5	0.74	0.75	0.51	0.90	0.53	0.02	0.01	0.01	0.02	0.02
uu	150	0.56	0.38	0.30	0.50	0.80	0.04	0.04	0.03	0.05	0.08
vv	5	0.74	0.75	0.51	0.90	0.13	0.02	0.01	0.01	0.02	0.01
vv	150	0.56	0.38	0.30	0.50	0.15	0.04	0.04	0.03	0.05	0.07
ww	5	0.74	0.75	0.51	0.90	0.20	0.02	0.01	0.01	0.02	0.02
ww	150	0.56	0.38	0.30	0.50	0.08	0.04	0.04	0.03	0.05	0.16

Table 4.11 Number of cells covered by integral length scales

	y^+	by L_x				by L_z			
		Mesh: 1	2	3	Periodic	Mesh: 1	2	3	Periodic
uu	5	4.7	6.0	5.1	7.2	0.41	0.26	0.33	0.52
uu	150	3.5	3.0	3.0	4.0	0.83	1.04	0.98	1.31
vv	5	4.7	6.0	5.1	7.2	0.41	0.26	0.33	0.52
vv	150	3.5	3.0	3.0	4.0	0.83	1.04	0.98	1.31
ww	5	4.7	6.0	5.1	7.2	0.41	0.26	0.33	0.52
ww	150	3.5	3.0	3.0	4.0	0.83	1.04	0.98	1.31

4.5.3 Energy spectra results

The third verification study for the mesh resolution is done based on the energy spectra and the details of this verification study are presented in Table 4.12. Energy spectra is also calculated using the times series of the streamwise velocity data at two points corresponding to y^+ values of 15 and 150. The objective in this verification analysis is to evaluate the influence of the mesh resolution on the energy spectra and to compare the spectra in the inertial subrange with the Kolmogorov spectrum.

Table 4.12 Details of the third verification test for the mesh resolution

Objective	Method of evaluation	Hypothesis	Expectation criteria
To verify the influence of the mesh resolution on power spectral density of the turbulent velocity field for the chosen SGS model	Comparison with Kolmogorov spectrum at inertial subrange	Convergence towards the Kolmogorov spectrum in the inertial subrange with mesh refinement	Asymptotic convergence of spectra to the Kolmogorov spectrum

The results of this verification analysis are presented in Figure 4.12. These results show a much less sensitive behavior of the energy spectra to the mesh resolution and this parameter therefore can does not prove to be useful as an indicator of the LES mesh resolution.

Figure 4.12 Energy spectra at two y^+ values

A visualization of the turbulent flow structures is also presented using the iso-surfaces of the

Q criterion in Figure 4.13. The Q criterion is the second invariant of the velocity gradient tensor. As expected from the computed values for the integral length scales, it can be seen that the eddies are more aligned in the streetwise direction.

$$Q = \frac{1}{2}[(tr(\nabla \boldsymbol{u}))^2 - tr(\nabla \boldsymbol{u}.\nabla \boldsymbol{u})] \tag{4.5}$$

Figure 4.13 Iso-surface of the Q criterion colored by the velocity magnitude

4.6 Discussion of channel case results

The channel flow test case was chosen due to its simple geometry, the available DNS data for it and since it characterizes flows with turbulent near wall behavior. For this case, several validation and verification studies were performed.

The verification analysis of the size of inlet eddies in the DFSEM boundary condition which is a method to generate synthetic turbulence at the inlet, shows the importance of the inlet eddy size at the inlet on the downstream flow development across the channel. As with the method in the original paper by Poletto et al. (2013) [65], the density of the eddies are defined as $d = \frac{\sigma_x \sigma_y \sigma_z N}{V_0}$, where σ values correspond to the eddy length scales in each direction, N being the number of eddies at the inlet and V_0 being the volume of the eddies. The paper emphasized the importance of the eddy density on the velocity field. This has been further investigated in this research, within the OpenFOAM implementation of the DFSEM method, which shows that inlet eddy size influences the downstream flow development as well as level of fluctuations in the flow. These observations were also confirmed by comparing the results to the results of the periodic case.

The validation analysis also showed the superior performance of the k-equation SGS model,

and a good performance of the WALE model, compared to the k-equation model, and inferior performance of the Smagorinsky model. Therefore for all other analysis of the channel flow, the k-equation model was used. For the sudden-expansion case, the WALE model is going to be used since it requires less computational time than k-equation and provides almost the same accuracy.

Further verification analysis were performed to investigate the influence of the mesh resolution for the channel flow. The results of the channel flow show adequate convergence behavior of the profiles of the averaged mean steam-wise velocity field and RMS of components of the velocity fluctuations. However, the results of the two-points autocorrelation show higher sensitivity to the mesh resolution. The results of the energy spectra, however, do not exhibit sensitivity to the mesh resolution. These results show that even for this simple geometry of the channel obtaining mesh-independent results is still challenging.

4.7   Dellenback Abrupt Expansion case description

The Dellenback Abrupt Expansion test case resembles the swirling flow inside the draft-tube of hydraulic turbines at part load condition. For this case, experimental data is presented for both axial and tangential velocity components of the turbulent swirling flow downstream of the 1:2 expansion. Measurements of mean and fluctuating velocities were performed in a water flow with a laser Doppler anemometer [79]. In the upstream tube, the Reynolds number was varied from 30,000 to 100,000 and the swirl number from zero to 1.2. The swirl number may be physically interpreted as the ratio of axial fluxes of swirl to linear momentum divided by a characteristic radius.

$$S = \frac{\int_0^{R_{in}} V_\theta V_z r^2 dr}{R_{in} \int_0^{R_{in}} V_z^2 r dr}\Big|_{z/D_{in}=-2.00} \tag{4.6}$$

The largest uncertainties in the experiments were reported to be about 2% in Reynolds number, 8% in swirl number, and 1% in probe volume positioning. Uncertainties in mean and RMS velocities stemming from the many possible biases and broadening errors were estimated to be about $\pm 3\%$ and $\pm 10\%$, respectively.

The geometry of the test case is shown in Figure 4.14 and and the geometry data is presented in Table 4.13. The measurement cases are presented in Table 4.14. The measurements were taken at the cross-sections shown in Figure 4.15.

Figure 4.14 Dellenback Abrupt Expansion geometry

This case has been studied also at the 4th OpenFOAM workshop. In this workshop the parametrized mesh was generated for this case using `m4` and `blockmesh`. This mesh is used for the simulations performed in this research. The mesh is shown in Figure 4.16. This mesh has 1567944 cells.

Table 4.13 Dellenback Abrupt Expansion geometric data

Inlet Diameter	D_{in}	50.78 mm
Outlet Diameter	D_{out}	98.5 mm
Expansion ratio	D_{out}/D_{in}	1.94
Inlet length	$2 \times D_{in}$	
Outlet length	$10 \times D_{in}$	

Table 4.14 Measurement cases

$Re = \frac{U_{b,in}D_{in}}{\nu}$	$S = \frac{\int_0^{R_{in}} V_\theta V_z r^2 dr}{R_{in}\int_0^{R_{in}} V_z^2 r dr}\big|_{z/D_{in}=-2.00}$
30,000	0.00, 0.60, 0.98
60,000	0.00, 1.16
100,000	0.00, 0.17, 0.74, 1.23

4.8 Boundary conditions and computational setup of sudden-expansion case

The boundary conditions applied for this case are summarized in Table 4.15 for RANS and in Table 4.16 for LES. The $k-\omega$ SST model is used as the turbulence model for the RANS and WALE model is used as the SGS model for the LES. In RANS, for all variables, the `Gauss linearUpwind` convection scheme is used which has a bounded first/second order numerical behavior. All schemes used for the LES are similar to the ones used for the channel flow simulations. For inlet boundary conditions, velocity profiles from the measurements are specified as axisymmetric profiles using the `profile1DfixedValue` boundary condition in OpenFOAM. For the case of simulations at swirl number 0.6, no inlet turbulence generation method is used, as it is stated in [80], the inlet turbulence is only important when the swirl in the flow is low. The simulations are performed at a Reynolds number of 30000.

Figure 4.15 Measurement cross-sections. Numbers refer to Z/D, where D is the inlet diameter, and Z=0 at the abrupt expansion

Figure 4.16 Numerical mesh for abrupt expansion test case

Table 4.15 OpenFOAM boundary condition for abrupt expansion case (RANS)

Variable	Inlet	Walls	Outlet
U	velocity profile from measurements	(0 0 0)	zeroGradient
p	zeroGradient	zeroGradient	fixedValue
k	$\frac{3}{2}(U_{b,in} \times 0.1)^2$	zeroGradient	zeroGradient
omega	$\sqrt{k}/(0.09 l_t)$	zeroGradient	zeroGradient
ν_t/ν	$k/(\omega\nu) = C_\mu k^2/(\epsilon\nu) \approx 16.3$	nutkWallFunction	zeroGradient

Table 4.16 OpenFOAM boundary condition for abrupt expansion case (LES)

Variable	Inlet	Walls	Outlet
U	velocity profile from measurements	(0 0 0)	zeroGradient
p	zeroGradient	zeroGradient	inletOutlet
ν_t/ν	$k/(\omega\nu) = C_\mu k^2/(\epsilon\nu) \approx 16.3$	zeroGradient	zeroGradient

4.9 Validation of mean and RMS of velocity components in sudden-expansion case

The validation study is performed to compare the results of the mean velocity field and RMS of velocity fluctuations against experimental data. These results for the axial and tangential components of the mean velocity at the aforementioned cross sections are presented and compared with experimental data in Figures 4.17 to 4.18. The same comparison is also drawn for the axial and tangential components of the RMS of the velocity fluctuations in Figures 4.19 to 4.20. The results of the LES WALE model show great improvement over the results of the RANS k-ω SST model. These results show a huge improvement in the mean velocity results compared to the RANS model, especially immediately after the expansion where $z/D = 0.25$ to $z/D = 1.5$. LES also captured the RMS of velocity components with a good agreement with experimental data. Three stages of the core vortex are visualized using the iso-surface of the pressure in Figure 4.21 which shows the ability of the LES to fully capture the generation and precessing of the core vortex inside the pipe.
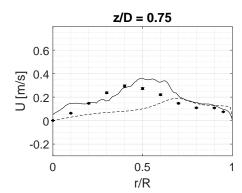
Figure 4.17 Mean axial velocity at several cross sections: comparison of RANS, LES and experiments (dashed line: k-ω SST RANS, solid line: WALE LES, dots: experiments)

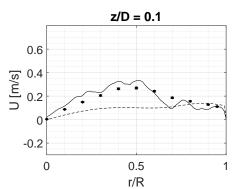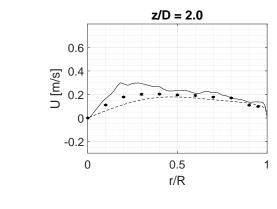Figure 4.18 Mean tangential velocity at several cross sections: comparison of RANS, LES and experiments (dashed line: k-ω SST RANS, solid line: WALE LES, dots: experiments)
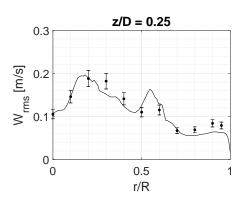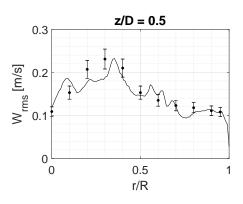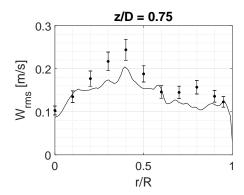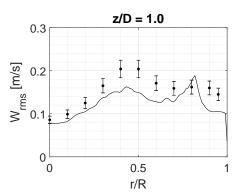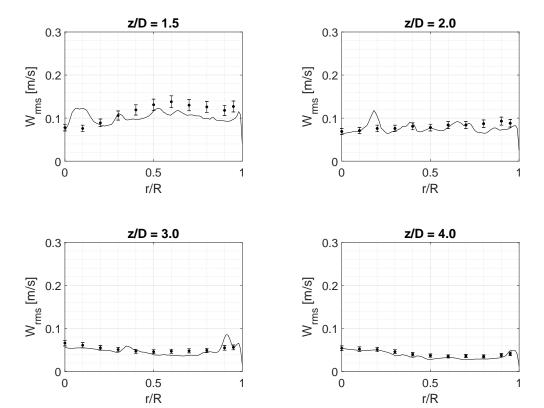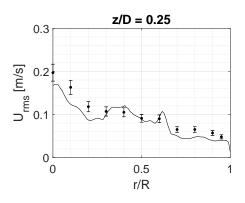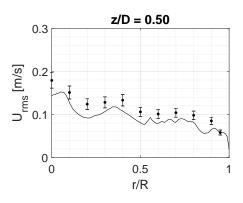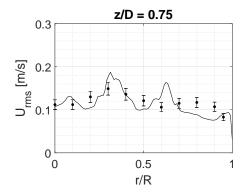
Figure 4.19 RMS of axial velocity at several cross sections: comparison of LES and experiments (solid line: WALE LES, dots: experiments)

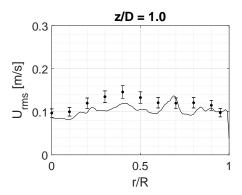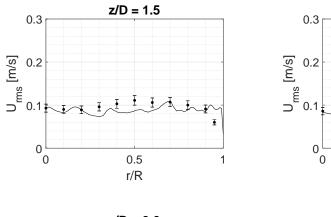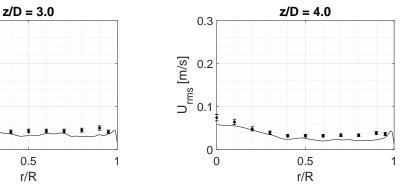Figure 4.20 RMS of tangential velocity at several cross sections: comparison of LES and experiments (solid line: WALE LES, dots: experiments)

Figure 4.21 Three stages of the core vortex visualized using iso-surface of the pressure

4.10 Verification of the mesh resolution for the sudden-expansion case

The verification analysis is performed to investigate the impact of the mesh resolution on the LES results. To this aim, two other meshes one coarser and one finer than the one for which results were presented in the previous section were generated. The details about these meshes are given in Table 4.17. The second mesh, which was used in the previous section, is further coarsened and refined in this section, and is the mesh on which RANS simulations are also performed. It is clear that with further refinement of the mesh, which leads to a number of 3 million cells, still the average value of the y^+ and its maximum value is higher than the value of 2 which is recommended for the LES. However, these meshes, which are chosen to maintain the reasonable calculation times, still yield results which show great improvement in comparison to the RANS ones.

Table 4.17 Details of the numerical grids for sudden expansion test case

Name	Number of cells	Δt	y^+_{min}	y^+_{max}	$y^+_{average}$
Mesh 1	787512	0.0005	0.195	35.42	5.29
Mesh 2	1567944	0.0005	0.360	28.70	4.21
Mesh 3	3108397	0.0001	0.412	54.17	6.38

The following sections cover the details of the three verification studies performed for this case. As with the channel case, for this case also the influence of the mesh resolution is investigated on the mean velocity field and RMS of velocity fluctuations, then on the two-points auto-correlations and finally on the energy spectrum of the pressure fluctuations.
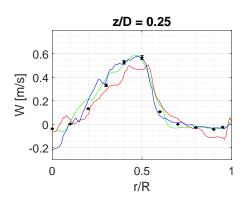
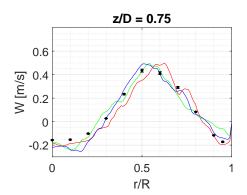### 4.10.1   Mean velocity and RMS of velocity fluctuations results

Details of the first verification study for the sudden-expansion case is given in Table 4.18. The aim of this study is to verify if we reach a converging behavior for the profiles of the mean and RMS velocities and if they can become independent of the mesh resolution.

Table 4.18 Details of the first verification test for the mesh resolution for the sudden expansion case

Objective	Method of evaluation	Hypothesis	Expectation criteria
To verify the influence of the mesh resolution on mean and RMS velocity components at cross sections	Asymptotic convergence behavior of the profiles within a range of uncertainty	Independence of the profiles from further mesh refinement	Asymptotic convergence of the profiles to experimental data

The results of these simulations are provided in Figure 4.22 to Figure 4.23 for the mean velocities for axial and tangential components and in Figure 4.24 to Figure 4.25 for RMS of velocity fluctuations, again for axial and tangential components. The results are, once again, given at the previously mentioned cross sections. These results show higher sensitivity of the velocity profiles to mesh resolution for both mean and RMS values. A higher mesh resolution does not necessarily give less deviation from experimental data, due to the complex nature of the flow, especially for RMS of velocity fluctuations. However, in general, results for Mesh 3 appear to be slightly more consistent with experimental data.

Figure 4.22 Mean axial velocity at several cross sections for different mesh resolutions (red: Mesh 1, green: Mesh 2, blue: Mesh 3, dots: experiments)

Figure 4.23 Mean tangential velocity at several cross sections for different mesh resolutions (red: Mesh 1, green: Mesh 2, blue: Mesh 3, dots: experiments)

Figure 4.24 RMS of axial velocity at several cross sections for different mesh resolutions (red: Mesh 1, green: Mesh 2, blue: Mesh 3, dots: experiments)

Figure 4.25 RMS of tangential velocity at several cross sections for different mesh resolutions (red: Mesh 1, green: Mesh 2, blue: Mesh 3, dots: experiments)

4.10.2 Two-point autocorrelation results

Details of the second verification study for the mesh resolution of the sudden-expansion case are given in Table 4.19. In this verification analysis we aimed at investigating the mesh resolution effect on the results of the two-point auto-correlation. The objective here is also to verify if we can get independent profiles of two-point auto-correlations from the mesh resolution or we can observe any converging behavior in the profiles. If so, we can calculate the integral length scales and verify that we are covering or not these scales with a sufficient number of cells.
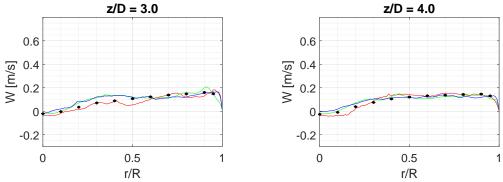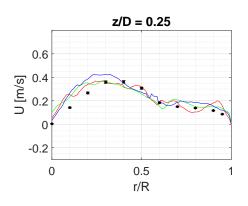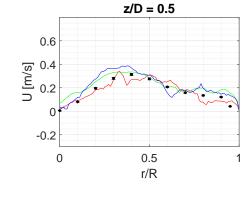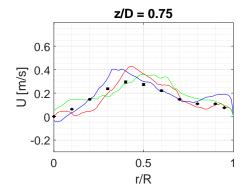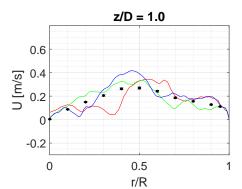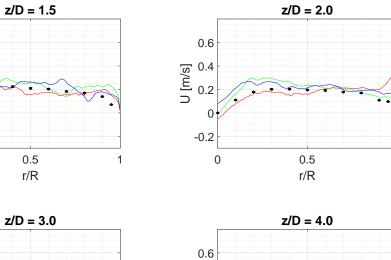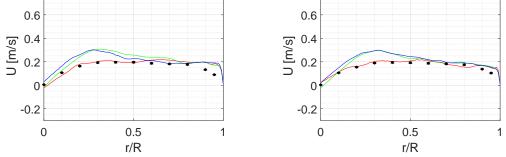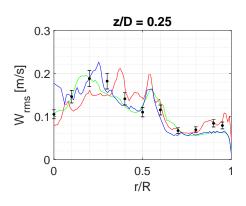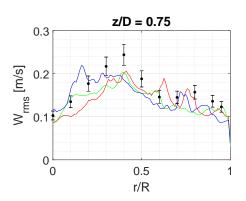
Table 4.19 Details of the second verification test for the mesh resolution for the sudden expansion case

Objective	Method of evaluation	Hypothesis	Expectation criteria
To verify the influence of the mesh resolution on spatial autocorrelation of fluctuations of the velocity at the centerline	Calculation of integral length scales	Independence of the integral length scales for a sufficient mesh resolution	Adequacy of a prescribed number of cells to cover integral length scales

The results of the two-point correlations of the components of the velocity fluctuations at the centerline of the cylinder downstream of the expansion is calculated for the three meshes. These results are presented in Figure 4.26. This figure shows that the complex vortical structures also represent a complex interactions which does not linearly goes to zero as it changes randomly further downstream of the expansion. This also illustrates the importance of further refining the mesh and taking into account the sensitivity of the results to the mesh resolution. Not being in the convergence zone and having large fluctuations in these profiles, calculation of the integral length scales will not make much sense here.

This is a clear indication that further mesh refinement would be required to ensure that computed solutions are independent of the mesh. Such refinement would however impose computation times which are beyond what would reasonably be achieved with currently available computational resources.

Figure 4.26 Two-point auto-correlation of the components of the velocity fluctuations along the centerline

4.10.3 Energy spectra results

The third verification analysis of the mesh resolution is performed for the results of the energy spectra of pressure fluctuations. Details of this verification study for the sudden-expansion case are given in Table 4.20. The objective of this analysis, as the case for the channel flow, is to investigate the effect of the mesh resolution on the convergence behavior of the energy spectra and also to compare the spectra in the inertial subrange with the Kolmogorov spectrum. Time history of the pressure fluctuations at several points at the wall is recorded and monitored during the simulations. Power spectral density of the pressure fluctuations at one point at $z/D = 2$ is calculated for the three meshes and results are presented in Figure 4.27. This case also shows less sensitivity of the results to the mesh resolution and this criteria can again not be used as an indicator of the mesh resolution adequacy.

Table 4.20 Details of the third verification test for the mesh resolution for the sudden expansion case

Objective	Method of evaluation	Hypothesis	Expectation criteria
To verify the influence of the mesh resolution on power spectral density of pressure fluctuations at a point at the wall	Comparison with Kolmogorov spectrum at inertial subrange	Convergence towards the Kolmogorov spectrum in the inertial subrange with mesh refinement	Asymptotic convergence of spectra to the Kolmogorov spectrum

Figure 4.27 Power spectral density of the pressure fluctuations at one point on the wall at $z/D = 2$

4.11   Discussion of sudden-expansion case results

In summary, the second test case which was chosen as the sudden-expansion case, resembles the swirling flow inside draft-tube of hydraulic turbines at their part load off-design operating conditions. For this case, experimental data was available for the mean velocity field and RMS of velocity fluctuations at several cross sections downstream of the expansion at various swirl and Reynolds numbers. The flow at Reynolds number of 30000 and swirl of 0.6 was chosen for this study.

As with the sudden-expansion case, the validation analysis of the LES WALE results versus RANS k-ω SST results show a large improvement of the LES results over RANS for the mean and RMS of axial and tangential velocities. These improvements were also more evident at the cross sections which were immediately after the expansion.

Moreover, the verification analysis of the mesh resolution show that the results are still mesh-dependent, which is due to the complex swirling flow downstream the expansion. The fluctuations in the RMS profiles are even larger than the mean profiles. The results of the two-point autocorrelation for this case show huge variations and we did not reach a convergence region. Further mesh refinement would be absolutely required for this case. The energy spectrum of the pressure fluctuations also did not exhibit much sensitivity to the mesh resolution, as it was also evident in the channel flow test case.

CHAPTER 5   CONCLUSION

This work is dedicated to developing an expertise on how to use, validate and verify the openFOAM CFD code for the large-eddy simulation of the flow types similar to the ones which occur at off-design operating condition such as part load inside hydraulic turbines.

5.1   Summary of Works

In order to fulfil the objective of this research, two main test cases, a case of turbulent channel flow and a case of sudden-expansion were considered in this study. The first one brings the classical problem of near-wall turbulence complexities and the second one resembles the swirling flow inside a hydraulic turbine draft-tube at part load off-design operating condition. Several SGS models were used and the results were compared among each other and to DNS data. Several indicators for the assessment of the mesh resolution for LES were identified and among them, two-point correlation and energy spectra were used to assess the impact of mesh resolution on LES results for the channel flow. The verified framework for LES on the channel flow was then applied to study the flow in sudden expansion pipe flow at a Reynolds number of 30000 and swirl number of 0.6. The results of this case show a large improvement compared to the results of RANS simulations. The influence of mesh resolution is further studied, which shows a higher sensitivity of the results of this case to the mesh resolution and characteristics.

5.2   Limitations

In this study, the OpenFOAM code is used for all simulations. The calculation of the identified mesh resolution indicators required the manipulation of the code to get the needed quantities, which therefore needed an in-depth understanding of the code and development of the expertise to use and further develop the code for post-processing without the need to import the data into another tool. Moreover, all these studies are also limited by the computation time and availability of resources in the context of this Master's research. Although other SGS models such as the dynamic model could have been used and verified, it was not the central aim of this research.

5.3   Future Research

The following are some possible research avenues steming from the work presented:

- To use the developed framework and expertise of this research for real cases of draft-tube or runner of hydraulic turbines at their off-design operating condition could be the next step in this research.

- To perform verification and validation analysis for other academic test cases as Timisoara Swirl Generator which includes guide vanes, runner and draft-tube would also be a step before proceeding to the actual turbine case.

- Also, developing a deeper understanding of the OpenFOAM code for further calculation of required fields for the assessment of the mesh resolution indicators such as LES index of quality could also be an important step to be taken.

- The impact of the other aspects of the LES calculations such as numerical schemes on the quality of the results would be also interesting to investigate.

- Explicit-filtering methods in large-eddy simulations for more in-depth analysis of mesh-dependency in LES analysis could also be investigated.

REFERENCES

[1] G. Tabor and M. Baba-Ahmadi, "Inlet conditions for large eddy simulation: A review," *Computers & Fluids*, vol. 39, no. 4, pp. 553–567, Apr. 2010. [Online]. Available: https://linkinghub.elsevier.com/retrieve/pii/S0045793009001601

[2] N. Jarrin, S. Benhamadouche, D. Laurence, and R. Prosser, "A synthetic-eddy-method for generating inflow conditions for large-eddy simulations," *International Journal of Heat and Fluid Flow*, vol. 27, no. 4, pp. 585–593, Aug. 2006. [Online]. Available: https://linkinghub.elsevier.com/retrieve/pii/S0142727X06000282

[3] "Key World Energy Statistics 2018."

[4] P. Dörfler, M. Sick, and A. Coutu, *Flow-Induced Pulsation and Vibration in Hydroelectric Machinery.* London: Springer London, 2013. [Online]. Available: http://link.springer.com/10.1007/978-1-4471-4252-2

[5] L. Davidson, *Fluid mechanics, turbulent flow and turbulence modeling*, 2018.

[6] *The Guide to Hydropower Mechanical Design.* PennWell Hydro Group, 2009, google-Books-ID: jSwkcgAACAAJ.

[7] A. T. Sayers, *Hydraulic and compressible flow turbomachines.* McGraw-Hill, Mar. 1990, google-Books-ID: YNpSAAAAMAAJ.

[8] K. Yamamoto, A. Müller, A. Favrel, and F. Avellan, "Experimental evidence of inter-blade cavitation vortex development in Francis turbines at deep part load condition," *Experiments in Fluids*, vol. 58, no. 10, Oct. 2017. [Online]. Available: http://link.springer.com/10.1007/s00348-017-2421-z

[9] C. Trivedi, M. J. Cervantes, and O. Gunnar Dahlhaug, "Numerical Techniques Applied to Hydraulic Turbines: A Perspective Review," *Applied Mechanics Reviews*, vol. 68, no. 1, p. 010802, Feb. 2016. [Online]. Available: http://appliedmechanicsreviews.asmedigitalcollection.asme.org/article.aspx?doi=10.1115/1.4032681

[10] C. Trivedi, "Compressible Large Eddy Simulation of a Francis Turbine During Speed-No-Load: Rotor Stator Interaction and Inception of a Vortical Flow," *Journal of Engineering for Gas Turbines and Power*, vol. 140, no. 11, p. 112601, Jun. 2018. [Online]. Available: http://gasturbinespower.asmedigitalcollection.asme.org/article.aspx?doi=10.1115/1.4039423

[11] C. Trivedi, E. Agnalt, and O. G. Dahlhaug, "Investigations of unsteady pressure loading in a Francis turbine during variable-speed operation," *Renewable Energy*, vol. 113, pp. 397–410, Dec. 2017. [Online]. Available: https://linkinghub.elsevier.com/retrieve/pii/S0960148117305062

[12] B. E. Launder and D. B. Spalding, *Lectures in mathematical models of turbulence.* Academic Press, 1979, google-Books-ID: 9e5QAAAAMAAJ.

[13] D. C. Wilcox, *Turbulence Modeling for CFD.* DCW Industries, 2006, google-Books-ID: q4ypAQAACAAJ.

[14] F. R. Menter, "Two-equation eddy-viscosity turbulence models for engineering applications," *AIAA Journal*, vol. 32, no. 8, pp. 1598–1605, Aug. 1994. [Online]. Available: http://arc.aiaa.org/doi/10.2514/3.12149

[15] P. Spalart and S. Allmaras, "A one-equation turbulence model for aerodynamic flows," in *30th Aerospace Sciences Meeting and Exhibit.* Reno,NV,U.S.A.: American Institute of Aeronautics and Astronautics, Jan. 1992. [Online]. Available: http://arc.aiaa.org/doi/10.2514/6.1992-439

[16] S. B. Pope, *Turbulent flows.* Cambridge ; New York: Cambridge University Press, 2000.

[17] P. Spalart, W.-H. Jou, and M. Strelets, "Comments on the feasability of LES for wings and on a hybrid RANS/LES approach." Louisiana Tech University: Greyden Press, 1997.

[18] A. Travin, M. Shur, M. Strelets, and P. R. Spalart, "Physical and Numerical Upgrades in the Detached-Eddy Simulation of Complex Turbulent Flows," in *Advances in LES of Complex Flows*, R. Friedrich and W. Rodi, Eds. Dordrecht: Kluwer Academic Publishers, 2004, vol. 65, pp. 239–254. [Online]. Available: http://link.springer.com/10.1007/0-306-48383-1_16

[19] L. Davidson and S. H. Peng, "Hybrid LES-RANS modelling: a one-equation SGS model combined with a k-w model for predicting recirculating flows," *International Journal for Numerical Methods in Fluids*, vol. 43, no. 9, pp. 1003–1018, Nov. 2003. [Online]. Available: http://doi.wiley.com/10.1002/fld.512

[20] F. Menter, M. Kuntz, and R. Bender, "A Scale-Adaptive Simulation Model for Turbulent Flow Predictions," in *41st Aerospace Sciences Meeting and Exhibit.* Reno,

Nevada: American Institute of Aeronautics and Astronautics, Jan. 2003. [Online]. Available: http://arc.aiaa.org/doi/10.2514/6.2003-767

[21] F. Menter and Y. Egorov, "A Scale Adaptive Simulation Model using Two-Equation Models," in *43rd AIAA Aerospace Sciences Meeting and Exhibit*. Reno, Nevada: American Institute of Aeronautics and Astronautics, Jan. 2005. [Online]. Available: http://arc.aiaa.org/doi/10.2514/6.2005-1095

[22] J. Smagorinsky, "General Circulation Experiments with the Primitive Equations: I. The Basic Experiment*," *Monthly Weather Review*, vol. 91, no. 3, pp. 99–164, Mar. 1963. [Online]. Available: http://journals.ametsoc.org/doi/abs/10.1175/1520-0493%281963%29091%3C0099%3AGCEWTP%3E2.3.CO%3B2

[23] J. W. Deardorff, "A numerical study of three-dimensional turbulent channel flow at large Reynolds numbers," *Journal of Fluid Mechanics*, vol. 41, no. 2, pp. 453–480, Apr. 1970. [Online]. Available: https://www.cambridge.org/core/product/identifier/S0022112070000691/type/journal_article

[24] G. D. Ciocan, M. S. Iliescu, T. C. Vu, B. Nennemann, and F. Avellan, "Experimental Study and Numerical Simulation of the FLINDT Draft Tube Rotating Vortex," *Journal of Fluids Engineering*, vol. 129, no. 2, p. 146, 2007. [Online]. Available: http://FluidsEngineering.asmedigitalcollection.asme.org/article.aspx?articleid=1430880

[25] T. C. Vu, C. Devals, Y. Zhang, B. Nennemann, and F. Guibault, "Steady and unsteady flow computation in an elbow dr aft tube with experimental validation," *IOP Conference Series: Earth and Environmental Science*, vol. 12, p. 012045, Aug. 2010. [Online]. Available: http://stacks.iop.org/1755-1315/12/i=1/a=012045?key=crossref.7622f3e1938145e0b0d1f99424f6cab9

[26] H. Foroutan and S. Yavuzkurt, "Simulation of flow in a simplified draft tube: turbulence closure considerations," *IOP Conference Series: Earth and Environmental Science*, vol. 15, no. 2, p. 022020, Nov. 2012. [Online]. Available: http://stacks.iop.org/1755-1315/15/i=2/a=022020?key=crossref.0ae620adf41e78c7b163df890aa8f29a

[27] J. Nicolle, J. F. Morissette, and A. M. Giroux, "Transient CFD simulation of a Francis turbine startup," *IOP Conference Series: Earth and Environmental Science*, vol. 15, no. 6, p. 062014, Nov. 2012. [Online]. Available: http://stacks.iop.org/1755-1315/15/i=6/a=062014?key=crossref.4df7544dc1fb7c58749c425989c90856

[28] E. Casartelli, L. Mangani, G. Romanelli, and T. Staubli, "Transient Simulation of Speed-No Load Conditions With An Open-Source Based C++ Code," *IOP Conference Series: Earth and Environmental Science*, vol. 22, no. 3, p. 032029, Mar. 2014. [Online]. Available: http://stacks.iop.org/1755-1315/22/i=3/a=032029?key=crossref. c00954271ef77c48f09e8c1a3f44421f

[29] C. Gentner, M. Sallaberger, C. Widmer, B.-J. Bobach, H. Jaberg, J. Schiffer, F. Senn, and M. Guggenberger, "Comprehensive experimental and numerical analysis of instability phenomena in pump turbines," *IOP Conference Series: Earth and Environmental Science*, vol. 22, no. 3, p. 032046, Mar. 2014. [Online]. Available: http://stacks.iop.org/1755-1315/22/i=3/a=032046?key=crossref. 416b1c3cbb2be5a4bab26bd249cda77d

[30] J. Nicolle, A. M. Giroux, and J. F. Morissette, "CFD configurations for hydraulic turbine startup," *IOP Conference Series: Earth and Environmental Science*, vol. 22, no. 3, p. 032021, Mar. 2014. [Online]. Available: http://stacks.iop.org/1755-1315/22/ i=3/a=032021?key=crossref.094e1e823905b490759572e27de91108

[31] H. Hosseinimanesh, C. Devals, B. Nennemann, M. Reggio, and F. Guibault, "A Numerical Study of Francis Turbine Operation at No-Load Condition," *Journal of Fluids Engineering*, vol. 139, no. 1, p. 011104, Nov. 2016. [Online]. Available: http: //fluidsengineering.asmedigitalcollection.asme.org/article.aspx?doi=10.1115/1.4034422

[32] A. D. A. Neto, R. Jester-Zuerker, A. Jung, and M. Maiwald, "Evaluation of a Francis turbine draft tube flow at part load using hybrid RANS-LES turbulence modelling," *IOP Conference Series: Earth and Environmental Science*, vol. 15, no. 6, p. 062010, Nov. 2012. [Online]. Available: http://stacks.iop.org/1755-1315/15/i=6/a= 062010?key=crossref.8d65c8198431949a72ab638b979a3662

[33] T. C. Vu, M. Gauthier, B. Nennemann, M. Koller, and C. Deschenes, "Flow simulation for a propeller turbine with different runner blade geometries," *IOP Conference Series: Earth and Environmental Science*, vol. 15, no. 3, p. 032004, Nov. 2012. [Online]. Available: http://stacks.iop.org/1755-1315/15/i=3/a=032004?key=crossref. f124d7f3700adbb7e6a1cf3e57d11571

[34] T. Krappel, A. Ruprecht, S. Riedelbauch, R. Jester-Zuerker, and A. Jung, "Investigation of Francis Turbine Part Load Instabilities using Flow Simulations with a Hybrid RANS-LES Turbulence Model," *IOP Conference Series: Earth and Environmental*

Science, vol. 22, no. 3, p. 032001, Mar. 2014. [Online]. Available: http://stacks.iop.org/ 1755-1315/22/i=3/a=032001?key=crossref.de21fa11beea59b5e8a87987ccb509cc

[35] T. Krappel, S. Riedelbauch, R. Jester-Zuerker, A. Jung, B. Flurl, F. Unger, and P. Galpin, "Turbulence Resolving Flow Simulations of a Francis Turbine in Part Load using Highly Parallel CFD Simulations," *IOP Conference Series: Earth and Environmental Science*, vol. 49, p. 062014, Nov. 2016. [Online]. Available: http://stacks. iop.org/1755-1315/49/i=6/a=062014?key=crossref.ec61973ee9e312cc7059109718a9b8af

[36] S. Pasche, F. Avellan, and F. Gallaire, "Part Load Vortex Rope as a Global Unstable Mode," *Journal of Fluids Engineering*, vol. 139, no. 5, p. 051102, Mar. 2017. [Online]. Available: http://fluidsengineering.asmedigitalcollection.asme.org/article.aspx?doi=10. 1115/1.4035640

[37] M. V. Magnoli and R. Schilling, "Numerical simulation of pressure pulsations in Francis turbines," *IOP Conference Series: Earth and Environmental Science*, vol. 15, no. 6, p. 062029, Nov. 2012. [Online]. Available: http://stacks.iop.org/1755-1315/15/i=6/a= 062029?key=crossref.b40333086bb3694a6f0d7ff177613032

[38] A. V. Sentyabov, A. A. Gavrilov, A. A. Dekterev, and A. V. Minakov, "Numerical investigation of the vortex core precession in a model hydro turbine with the aid of hybrid methods for computation of turbulent flows," *Thermophysics and Aeromechanics*, vol. 21, no. 6, pp. 707–718, Dec. 2014. [Online]. Available: http://link.springer.com/10.1134/S0869864314060055

[39] J. Paik, F. Sotiropoulos, and M. J. Sale, "Numerical Simulation of Swirling Flow in Complex Hydroturbine Draft Tube Using Unsteady Statistical Turbulence Models," *Journal of Hydraulic Engineering*, vol. 131, no. 6, pp. 441–456, Jun. 2005. [Online]. Available: http://ascelibrary.org/doi/10.1061/%28ASCE%290733-9429%282005% 29131%3A6%28441%29

[40] A. Minakov, D. Platonov, A. Dekterev, A. Sentyabov, and A. Zakharov, "The analysis of unsteady flow structure and low frequency pressure pulsations in the high-head Francis turbines," *International Journal of Heat and Fluid Flow*, vol. 53, pp. 183–194, Jun. 2015. [Online]. Available: http://linkinghub.elsevier.com/retrieve/pii/S0142727X15000296

[41] A. Taheri, "Detached Eddy Simulation of Unsteady Turbulent Flows in the Draft Tube of a Bulb Turbine," Ph.D. dissertation, 2015.

[42] C. Duprat, O. Métais, and T. Laverne, "Large Eddy Simulation of a High Reynolds Number Swirling Flow in a Conical Diffuser," *International Journal of Fluid Machinery and Systems*, p. 7, 2009.

[43] D. Jošt and A. Lipej, "Numerical Prediction of Non-Cavitating and Cavitating Vortex Rope in a Francis Turbine Draft Tube," *Strojniški vestnik – Journal of Mechanical Engineering*, vol. 57, no. 06, pp. 445–456, Jun. 2011.

[44] W. T. Su, X. B. Li, F. C. Li, W. F. Han, X. Z. Wei, and J. Guo, "Large eddy simulation of pressure fluctuations at off-design condition in a Francis turbine based on cavitation model," *IOP Conference Series: Materials Science and Engineering*, vol. 52, no. 2, p. 022032, Dec. 2013. [Online]. Available: http://stacks.iop.org/1757-899X/52/i=2/a=022032?key=crossref.0505a8fbbd76de7aa01c092827fca967

[45] A. Javadi and H. Nilsson, "A comparative study of scale-adaptive and large-eddy simulations of highly swirling turbulent flow through an abrupt expansion," *IOP Conference Series: Earth and Environmental Science*, vol. 22, no. 2, p. 022017, Mar. 2014. [Online]. Available: http://stacks.iop.org/1755-1315/22/i=2/a=022017?key=crossref.3a37fe0ce241e44d5a076d78c35fbe46

[46] O. Pacot, C. Kato, and F. Avellan, "High-resolution LES of the rotating stall in a reduced scale model pump-turbine," *IOP Conference Series: Earth and Environmental Science*, vol. 22, no. 2, p. 022018, Mar. 2014. [Online]. Available: http://stacks.iop.org/1755-1315/22/i=2/a=022018?key=crossref.6173bb8db8fada7ca9a4c6ff3b5ca483

[47] M. Morgut, D. Jošt, E. Nobile, and A. Škerlavaj, "Numerical investigation of the flow in axial water turbines and marine propellers with scale-resolving simulations," *Journal of Physics: Conference Series*, vol. 655, p. 012052, Nov. 2015. [Online]. Available: http://stacks.iop.org/1742-6596/655/i=1/a=012052?key=crossref.62bbd5856f125e91f52bdc01bad0ea5d

[48] O. Pacot, C. Kato, Y. Guo, and Y. Yamade, "Prediction of the Pressure Pulsation in a Draft Tube for a Part Load Condition Using the LES Approach," p. 8, 2015.

[49] C. Mende, W. Weber, and U. Seidel, "Progress in load prediction for speed-no-load operation in Francis turbines," *IOP Conference Series: Earth and Environmental Science*, vol. 49, p. 062017, Nov. 2016. [Online]. Available: http://stacks.iop.org/1755-1315/49/i=6/a=062017?key=crossref.3a3330a2366d451bc4794530179aa426

[50] S. Wilhelm, G. Balarac, O. Métais, and C. Ségoufin, "Head losses prediction and analysis in a bulb turbine draft tube under different operating conditions using unsteady simulations," *IOP Conference Series: Earth and Environmental Science*, vol. 49, p. 022010, Nov. 2016. [Online]. Available: http://stacks.iop.org/1755-1315/49/i=2/a=022010?key=crossref.a6a2e0e85542cbe67d05664a0acd15f3

[51] S. Wilhelm, G. Balarac, O. Metais, and C. Segoufin, "Analysis of Head Losses in a Turbine Draft Tube by Means of 3d Unsteady Simulations," *Flow, Turbulence and Combustion*, vol. 97, no. 4, pp. 1255–1280, Dec. 2016. [Online]. Available: http://link.springer.com/10.1007/s10494-016-9767-9

[52] J. Yang, L. Zhou, and Z. Wang, "The numerical simulation of draft tube cavitation in Francis turbine at off-design conditions," *Engineering Computations*, vol. 33, no. 1, pp. 139–155, Mar. 2016. [Online]. Available: http://www.emeraldinsight.com/doi/10.1108/EC-12-2014-0257

[53] A. Minakov, D. Platonov, A. Sentyabov, and A. Gavrilov, "Francis-99 turbine numerical flow simulation of steady state operation using RANS and RANS/LES turbulence model," *Journal of Physics: Conference Series*, vol. 782, p. 012005, Jan. 2017. [Online]. Available: http://stacks.iop.org/1742-6596/782/i=1/a=012005?key=crossref.366806df7d7dc2e65e8ef984b7c3cf19

[54] A. V. Minakov, D. V. Platonov, I. V. Litvinov, S. I. Shtork, and K. Hanjalić, "Vortex ropes in draft tube of a laboratory Kaplan hydroturbine at low load: an experimental and LES scrutiny of RANS and DES computational models," *Journal of Hydraulic Research*, vol. 55, no. 5, pp. 668–685, Sep. 2017. [Online]. Available: https://www.tandfonline.com/doi/full/10.1080/00221686.2017.1300192

[55] C. Trivedi and O. G. Dahlhaug, "Interaction between trailing edge wake and vortex rings in a Francis turbine at runaway condition: Compressible large eddy simulation," *Physics of Fluids*, vol. 30, no. 7, p. 075101, Jul. 2018. [Online]. Available: http://aip.scitation.org/doi/10.1063/1.5030867

[56] A. Javadi and H. Nilsson, "Detailed numerical investigation of a Kaplan turbine with rotor-stator interaction using turbulence-resolving simulations," *International Journal of Heat and Fluid Flow*, vol. 63, pp. 1–13, Feb. 2017. [Online]. Available: http://linkinghub.elsevier.com/retrieve/pii/S0142727X16307603

[57] A. Gavrilov, A. Sentyabov, A. Dekterev, and K. Hanjalić, "Vortical structures and pressure pulsations in draft tube of a Francis-99 turbine at part load:

RANS and hybrid RANS/LES analysis," *International Journal of Heat and Fluid Flow*, vol. 63, pp. 158–171, Feb. 2017. [Online]. Available: http://linkinghub.elsevier.com/retrieve/pii/S0142727X16301886

[58] T. Krappel, H. Kuhlmann, O. Kirschner, A. Ruprecht, and S. Riedelbauch, "Validation of an IDDES-type turbulence model and application to a Francis pump turbine flow simulation in comparison with experimental results," *International Journal of Heat and Fluid Flow*, vol. 55, pp. 167–179, 2015. [Online]. Available: http://linkinghub.elsevier.com/retrieve/pii/S0142727X15001010

[59] H. Foroutan and S. Yavuzkurt, "A partially-averaged Navier–Stokes model for the simulation of turbulent swirling flow with vortex breakdown," *International Journal of Heat and Fluid Flow*, vol. 50, pp. 402–416, Dec. 2014. [Online]. Available: http://linkinghub.elsevier.com/retrieve/pii/S0142727X14001301

[60] D. Jošt, A. Škerlavaj, and A. Lipej, "Improvement of Efficiency Prediction for a Kaplan Turbine with Advanced Turbulence Models," *Strojniški vestnik – Journal of Mechanical Engineering*, vol. 60, no. 2, pp. 124–134, Feb. 2014.

[61] D. Jošt and A. Škerlavaj, "Efficiency prediction for a low head bulb turbine with SAS SST and zonal LES turbulence models," *IOP Conference Series: Earth and Environmental Science*, vol. 22, no. 2, p. 022007, 2014.

[62] F. Nicoud and F. Ducros, "Subgrid-Scale Stress Modelling Based on the Square of the Velocity Gradient Tensor," vol. 62, pp. 183–200, 1999.

[63] M. Germano, U. Piomelli, P. Moin, and W. H. Cabot, "A dynamic subgrid-scale eddy viscosity model," *Physics of Fluids A: Fluid Dynamics*, vol. 3, no. 7, pp. 1760–1765, Jul. 1991. [Online]. Available: http://aip.scitation.org/doi/10.1063/1.857955

[64] D. K. Lilly, "A proposed modification of the Germano subgrid-scale closure method," *Physics of Fluids A: Fluid Dynamics*, vol. 4, no. 3, pp. 633–635, Mar. 1992. [Online]. Available: http://aip.scitation.org/doi/10.1063/1.858280

[65] R. Poletto, T. Craft, and A. Revell, "A New Divergence Free Synthetic Eddy Method for the Reproduction of Inlet Flow Conditions for LES," p. 21, 2013.

[66] N. Jarrin, R. Prosser, J.-C. Uribe, S. Benhamadouche, and D. Laurence, "Reconstruction of turbulent fluctuations for hybrid RANS/LES simulations using a Synthetic-Eddy Method," *International Journal of Heat and Fluid*

Flow, vol. 30, no. 3, pp. 435–442, Jun. 2009. [Online]. Available: https://linkinghub.elsevier.com/retrieve/pii/S0142727X09000538

[67] S. E. Gant, "Reliability Issues of LES-Related Approaches in an Industrial Context," *Flow, Turbulence and Combustion*, vol. 84, no. 2, pp. 325–335, 2010. [Online]. Available: http://link.springer.com/10.1007/s10494-009-9237-8

[68] I. Celik, M. Klein, M. Freitag, and J. Janicka, "Assessment measures for URANS/DES/LES: an overview with applications," *Journal of Turbulence*, vol. 7, p. N48, Jan. 2006. [Online]. Available: http://www.tandfonline.com/doi/abs/10.1080/14685240600794379

[69] I. B. Celik, Z. N. Cehreli, and I. Yavuz, "Index of Resolution Quality for Large Eddy Simulations," *Journal of Fluids Engineering*, vol. 127, no. 5, p. 949, 2005. [Online]. Available: http://FluidsEngineering.asmedigitalcollection.asme.org/article.aspx?articleid=1430215

[70] L. Davidson, "Large Eddy Simulations: How to evaluate resolution," *International Journal of Heat and Fluid Flow*, vol. 30, no. 5, pp. 1016–1025, Oct. 2009. [Online]. Available: https://linkinghub.elsevier.com/retrieve/pii/S0142727X09001039

[71] M. V. Salvetti, Ed., *Quality and reliability of large-eddy simulations II: the second workshop on "Quality and Reliability of Large-Eddy Simulations", QLES2009, was held at the University of Pisa from September 9 to September 11, 2009*, ser. ERCOFTAC series. Dordrecht: Springer, 2011, no. 16, oCLC: 837896204.

[72] S. B. Pope, "Ten questions concerning the large-eddy simulation of turbulent flows," *New Journal of Physics*, vol. 6, pp. 35–35, Mar. 2004. [Online]. Available: http://stacks.iop.org/1367-2630/6/i=1/a=035?key=crossref.52a7b24a34f388e291ce7d86a724556b

[73] B. J. Geurts and J. Fröhlich, "A framework for predicting accuracy limitations in large-eddy simulation," *Physics of Fluids*, vol. 14, no. 6, pp. L41–L44, Jun. 2002. [Online]. Available: http://aip.scitation.org/doi/10.1063/1.1480830

[74] I. Celik, M. Klein, and J. Janicka, "Assessment Measures for Engineering LES Applications," *Journal of Fluids Engineering*, vol. 131, no. 3, p. 031102, 2009. [Online]. Available: http://FluidsEngineering.asmedigitalcollection.asme.org/article.aspx?articleid=1478229

[75] M. Klein, "An Attempt to Assess the Quality of Large Eddy Simulations in the Context of Implicit Filtering," *Flow, Turbulence and Combustion*, vol. 75, no. 1-4, pp. 131–147, Dec. 2005. [Online]. Available: http://link.springer.com/10.1007/s10494-005-8581-6

[76] W. L. Oberkampf and T. G. Trucano, "Verification and validation in computational fluid dynamics," *Progress in Aerospace Sciences*, p. 64, 2002.

[77] Computational Fluid Dynamics Committee, Ed., *Guide: Guide for the Verification and Validation of Computational Fluid Dynamics Simulations (AIAA G-077-1998(2002))*. Washington, DC: American Institute of Aeronautics and Astronautics, Inc., Jan. 1998. [Online]. Available: http://arc.aiaa.org/doi/book/10.2514/4.472855

[78] R. D. Moser, J. Kim, and N. N. Mansour, "Direct numerical simulation of turbulent channel flow up to Re590," p. 3, 1999.

[79] P. A. Dellenback, D. E. Metzger, and G. P. Neitzel, "Measurements in turbulent swirling flow through an abrupt axisymmetric expansion," *AIAA Journal*, vol. 26, no. 6, pp. 669–681, Jun. 1988. [Online]. Available: http://arc.aiaa.org/doi/10.2514/3.9952

[80] J. U. Schlüter, H. Pitsch, and P. Moin, "Large-Eddy Simulation Inflow Conditions for Coupling with Reynolds-Averaged Flow Solvers," *AIAA Journal*, vol. 42, no. 3, pp. 478–484, Mar. 2004. [Online]. Available: https://arc.aiaa.org/doi/10.2514/1.3488

[81] E. de Villiers, "The Potential of Large Eddy Simulation for the Modeling of Wall Bounded Flows," p. 375.

APPENDIX A   OPENFOAM TEST CASE SETUP

OpenFOAM (Open Field Operation And Manipulation) is an open source, free CFD code. OpenFOAM consists of C++ libraries, which foremost are used to create applications which consist of solvers and utilities. The solvers are each designed to solve a specific problem in computational continuum mechanics; and the utilities that perform simple pre-and post-processing tasks, mainly involving data manipulation and algebraic calculations. The solvers and utilities are controlled through the use of dictionaries. These are files where specifications of the applications are accessed and controlled. Specifications such as discretization schemes, simulation time steps, divergence schemes, turbulence models, pressure corrector settings, and linear solver settings are all controlled through these sets of dictionaries. OpenFOAM uses a common structure to set up a problem. The basic directory structure for a OpenFOAM case directories which are necessary to create a case in OpenFOAM is given in Figure A.1. When the solver is running, it initiates the computations with the values given in a `0` directory, as in time 0. Then it prints the quantity fields in time directories, with a time interval specified in a dictionary called `controlDict` located in directory `system`. Two other files in the system directory are `fvSolution` and `fvSchemes` which include information on solver settings (tolerances, under-relaxation factors, etc.) and numerical schemes, respectively. Information about computational grid, turbulence model, and material properties are given in `constant` directory.

The OpenFOAM keyword for implicit second-order backward time scheme is `backward` which is specified value for `ddtSchemes`. Linear interpolation schemes are used to transform cell-centre quantities to face centres. The cell gradients are calculated using least squares method with `leastSquares` syntax in OpenFOAM.

Many of the convection schemes in OpenFOAM are based on the Normalised Variable (NV) and Total Variation Diminishing (TVD) methods. These provide a set of tools to characterise scheme properties such as boundedness (1-D). These schemes offer a blend between a low order scheme and a higher order scheme based on the calculation of a limiter. The boundedness can be improved in 2-D and 3-D cases by limiting the gradient.

Linear divergence scheme which is an NV (Normalised Variable) unbounded with second-order accuracy method, is used for the calculation of the convection of the velocity. The OpenFOAM syntax is `Gauss linear` which mean Gauss theorem is also used. Limited linear divergence scheme (`Gauss limitedLinear`) which has a blend between first and second order methods, and is a TVD method, is applied to calculate the convection of the subgrid scale
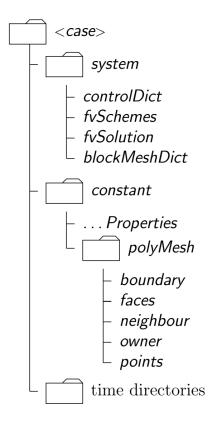
Figure A.1 Case directory structure

turbulent kinetic energy, whenever the k-equation method is used as an SGS model.

The surface-normal contribution of a property at a face can can be interpolated from the cell-based gradient. For that central-difference scheme without non-orthogonal correction with syntax of `uncorrected` for `snGradSchemes`. Laplacian schemes are based on the application of Gauss theorem, requiring an interpolation scheme and a surface-normal gradient scheme. Therefore we have `Gauss linear uncorrected` specified for `laplacianSchemes`.

The solver `pimpleFoam`, provided as part of OpenFOAM, was used to solve the equations. The algorithm implemented in the solver is based on a blend of the transient SIMPLE (Semi-Implicit Method for Pressure-Linked Equations) and PISO (Pressure Implicit with Splitting of Operators) algorithms. The steps in `pimpleFoam` solver once presented in Figure 3.3. At the beginning of each time-step, the algorithm increases the current simulation time by the value of the time-step. Then the pressure-velocity coupling loop is executed. Inside the loop, the momentum equation is solved first, after which the corrector loop is entered. Inside the corrector loop, the pressure equation is solved and the velocity field is corrected ensuring that it is divergence free. Here we have `nOuterCorrectors` in OpenFOAM which identifies

the number of times for re-calculation of the pressure-momentum coupling and `nCorrectors` for the number of times for pressure correction. Finally, all equations related to turbulence modelling are solved.

To solve the system of alegbraic equations a set of linear solvers are available in Open-FOAM. Geometric agglomerated algebraic multigrid solver (GAMG) with combined DIC (Diagonal-based Incomplete Cholesky) and Gauss Seidel Smoother (`DICGaussSeidel`) is used to pressure equations. Momentum and turbulence equations are solved using smooth solver (`smoothSolver`) with symmetric Gauss Seidel Smoother (`symGaussSeidel`).

A.1 Discretization methods and solver setup for the channel flow case

A summary of the OpenFOAM solver setup for spatial and temporal derivatives and variables for the channel flow case are given in Tables A.1, A.2 and A.3.

For the periodic case, the corresponding pressure gradient to force the flow through the channel is specified using a source as mean velocity force (`meanVelocityForce`) which calculates a momentum source so that the volume averaged velocity in the whole computational domain (`all` keyword in OpenFOAM) reaches the desired mean velocity `Ubar`. This source is specified in the file `fvOptions`.

Table A.1 OpenFOAM setup

type	details
transportModel	Newtonian $\nu = 2.532 \times 10^{-3} \ [\frac{m^2}{s^2}]$
LESModel	kEquation ($C_k = 0.02655$, $C_e = 1.048$), delta (vanDriest)
ddtSchemes	backward
gradSchemes	leastSquares
div (phi,U)	Gauss linear
div (phi,k)	Gauss limitedLinear 0.1
div ((nuEff*dev2(T(grad(U)))))	Gauss linear
laplacianSchemes	Gauss linear uncorrected
interpolationSchemes	linear
snGradSchemes	uncorrected

It is worth mentioning that the simulation with the periodic boundary conditions for the inlet and outlet were initialized by using an initial turbulent field generated by using an OpenFOAM utility called `perturbU`. These utilities were created by Eugene de Villiers [81]. The `perturbUDict` requires the input value for the friction Reynolds number (Re_τ) and some constants.

Table A.2 OpenFOAM solver setup

Field	solver	smoother	tolerance	relTol
p	GAMG	DICGaussSeidel	0	0.1
pFinal	GAMG	DICGaussSeidel	1×10^{-6}	0
(U|k)	smoothSolver	symGaussSeidel	1×10^{-5}	0.1
(U|k)Final	smoothSolver	symGaussSeidel	1×10^{-6}	0

Table A.3 OpenFOAM PIMPLE setup

nOuterCorrectors	3
nCorrectors	1
nNonOrthogonalCorrectors	0

A.2 Examples of dictionary files in OpenFOAM

In this section examples of the dictionary files in OpenFOAM are provided. The followings are examples of file content of `blockMeshDict` which is used for the mesh generation inside channel, `controlDict`, `fvSchemes` and `fvSolution` dictionaries.

Example of `blockMeshDict`:

```
1  /*--------------------------------*- C++ -*----------------------------------*\
2  | =========                 |                                                 |
3  | \\      /  F ield          | OpenFOAM: The Open Source CFD Toolbox           |
4  | \\    /   O peration       | Version:  plus                                  |
5  | \\  /    A nd              | Web:      www.OpenFOAM.com                       |
6  | \\/     M anipulation      |                                                 |
7  \*---------------------------------------------------------------------------*/
8  FoamFile
9  {
10      version    2.0;
11      format     ascii;
12      class      dictionary;
13      object     blockMeshDict;
14  }
15  // * * * * * * * * * * * * * * * * * * * * * * * * * * * * * * * * * * * * * //
16
17  scale    1;
18
19  L #calc "20*M_PI";
20  H #calc "1";
21  H2 #calc "2*$H";
22  W #calc "M_PI";
23
24  vertices
25  (
26      ( 0   0   0)
```

```
27      ($L    0    0)
28      ($L   $H    0)
29      ($L  $H2    0)
30      ( 0  $H2    0)
31      ( 0   $H    0)
32
33      ( 0    0   $W)
34      ($L    0   $W)
35      ($L   $H   $W)
36      ($L  $H2   $W)
37      ( 0  $H2   $W)
38      ( 0   $H   $W)
39  );
40
41  blocks
42  (
43      hex ( 0   1   2   5   6   7   8  11) (500 23 82) simpleGrading (1 25 1)
44      hex ( 5   2   3   4  11   8   9  10) (500 23 82) simpleGrading (1 0.04 1)
45  );
46
47  edges
48  (
49  );
50
51  boundary
52  (
53      bottomWall
54      {
55          type            wall;
56          faces           ((0 6 7 1));
57      }
58      topWall
59      {
60          type            wall;
61          faces           ((4 3 9 10));
62      }
63
64      sides_half0
65      {
66          type            cyclic;
67          neighbourPatch  sides_half1;
68          faces           ((1 2 5 0)(2 3 4 5));
69      }
70      sides_half1
71      {
72          type            cyclic;
73          neighbourPatch  sides_half0;
74          faces           ((6 11 8 7)(11 10 9 8));
75      }
76
77
78      inlet
79      {
80          type            patch;
81          faces           ((0 5 11 6)(5 4 10 11));
```

```
82        }
83        outlet
84        {
85            type            patch;
86            faces           ((1 7 8 2)(2 8 9 3));
87        }
88  );
89
90  mergePatchPairs
91  (
92  );
93
94  // ************************************************************************* //
```

Example of `controlDict`:

```
1   /*--------------------------------*- C++ -*----------------------------------*\
2   | =========                 |                                                 |
3   | \\      /  F ield         | OpenFOAM: The Open Source CFD Toolbox           |
4   |  \\    /   O peration      | Version:   plus                                 |
5   |   \\  /    A nd           | Web:       www.OpenFOAM.com                      |
6   |    \\/     M anipulation  |                                                 |
7   \*---------------------------------------------------------------------------*/
8   FoamFile
9   {
10      version     2.0;
11      format      ascii;
12      class       dictionary;
13      location    "system";
14      object      controlDict;
15  }
16  // * * * * * * * * * * * * * * * * * * * * * * * * * * * * * * * * * * * * * * //
17
18  application     pimpleFoam;
19
20  startFrom       startTime;
21
22  startTime       0;
23
24  stopAt          endTime;
25
26  endTime         85;
27
28  deltaT          4e-3;
29
30  writeControl    timeStep;
31
32  writeInterval   25;
33
34  purgeWrite      10;
35
36  writeFormat     ascii;
37
38  writePrecision  6;
39
```

```
40  writeCompression off;
41
42  timeFormat      general;
43
44  timePrecision   6;
45
46  runTimeModifiable true;
47
48  functions
49  {
50      Q1
51      {
52          type            Q;
53          libs            ("libfieldFunctionObjects.so");
54          writeControl    writeTime;
55      }
56      vorticity1
57      {
58          type            vorticity;
59          libs            ("libfieldFunctionObjects.so");
60          writeControl    writeTime;
61      }
62      yPlus
63      {
64          type            yPlus;
65          libs            ("libfieldFunctionObjects.so");
66          writeControl    writeTime;
67      }
68      fieldAverage1
69      {
70          type            fieldAverage;
71          libs            ("libfieldFunctionObjects.so");
72          writeControl    writeTime;
73          timeStart       8.5;
74
75          fields
76          (
77              U
78              {
79                  mean        on;
80                  prime2Mean  on;
81                  base        time;
82              }
83
84              p
85              {
86                  mean        on;
87                  prime2Mean  on;
88                  base        time;
89              }
90          );
91      }
92  }
93
94
```

```
// ************************************************************************* //
```

Example of `fvSchemes`:

```cpp
/*--------------------------------*- C++ -*----------------------------------*\
| =========                 |                                                 |
| \\      /  F ield         | OpenFOAM: The Open Source CFD Toolbox           |
|  \\    /   O peration     | Version:  plus                                  |
|   \\  /    A nd           | Web:      www.OpenFOAM.com                      |
|    \\/     M anipulation  |                                                 |
\*---------------------------------------------------------------------------*/
FoamFile
{
    version     2.0;
    format      ascii;
    class       dictionary;
    location    "system";
    object      fvSchemes;
}
// * * * * * * * * * * * * * * * * * * * * * * * * * * * * * * * * * * * * * //

ddtSchemes
{
    default         backward;
}

gradSchemes
{
    default         leastSquares;
}

divSchemes
{
    default         none;
    div(phi,U)      Gauss linear;
    div(phi,k)      Gauss limitedLinear 0.1;
    div(phi,B)      Gauss limitedLinear 0.1;
    div(B)          Gauss linear;
    div(phi,nuTilda) Gauss limitedLinear 0.1;
    div((nuEff*dev2(T(grad(U))))) Gauss linear;
}

laplacianSchemes
{
    default         Gauss linear uncorrected;
}

interpolationSchemes
{
    default         linear;
}

snGradSchemes
{
    default         uncorrected;
```

```
52   }
53
54
55   // ************************************************************************* //
```

Example of `fvSolution`:

```
1    /*--------------------------------*- C++ -*----------------------------------*\
2    | =========                 |                                                 |
3    | \\      /  F ield          | OpenFOAM: The Open Source CFD Toolbox           |
4    | \\    /   O peration        | Version:  plus                                 |
5    |  \\  /    A nd             | Web:      www.OpenFOAM.com                      |
6    |   \\/     M anipulation    |                                                 |
7    \*---------------------------------------------------------------------------*/
8    FoamFile
9    {
10       version     2.0;
11       format      ascii;
12       class       dictionary;
13       location    "system";
14       object      fvSolution;
15   }
16   // * * * * * * * * * * * * * * * * * * * * * * * * * * * * * * * * * * * * * //
17
18   solvers
19   {
20       p
21       {
22           solver          GAMG;
23           tolerance       0;
24           relTol          0.01;
25           smoother        DICGaussSeidel;
26           nPreSweeps      0;
27           nPostSweeps     2;
28           cacheAgglomeration true;
29           nCellsInCoarsestLevel 10;
30           agglomerator    faceAreaPair;
31           mergeLevels     1;
32       }
33
34       pFinal
35       {
36           $p;
37           smoother        DICGaussSeidel;
38           tolerance       1e-06;
39           relTol          0;
40       }
41
42       "(U|k)"
43       {
44           solver          smoothSolver;
45           smoother        symGaussSeidel;
46           tolerance       1e-05;
47           relTol          0.1;
48           minIter         1;
```

```
49        }
50
51        "(U|k)Final"
52        {
53            $U;
54            tolerance        1e-06;
55            relTol           0;
56        }
57   }
58
59   PIMPLE
60   {
61        nOuterCorrectors 3;
62        nCorrectors      1;
63        nNonOrthogonalCorrectors 0;
64   }
65
66
67   // ************************************************************************* //
```